ARTICLE

https://doi.org/10.1038/s41586-019-1506-7

Conserved cell types with divergent features in human versus mouse cortex

Rebecca D. Hodge[1,13], Trygve E. Bakken[1,13], Jeremy A. Miller[1], Kimberly A. Smith[1], Eliza R. Barkan[1], Lucas T. Graybuck[1], Jennie L. Close[1], Brian Long[1], Nelson Johansen[2], Osnat Penn[1], Zizhen Yao[1], Jeroen Eggermont[3], Thomas Höllt[3,4], Boaz P. Levi[1], Soraya I. Shehata[1], Brian Aevermann[5], Allison Beller[6], Darren Bertagnolli[1], Krissy Brouner[1], Tamara Casper[1], Charles Cobbs[7], Rachel Dalley[1], Nick Dee[1], Song-Lin Ding[1], Richard G. Ellenbogen[8], Olivia Fong[1], Emma Garren[1], Jeff Goldy[1], Ryder P. Gwinn[9], Daniel Hirschstein[1], C. Dirk Keene[6], Mohamed Keshk[5], Andrew L. Ko[8,10], Kanan Lathia[1], Ahmed Mahfouz[3,4], Zoe Maltzer[1], Medea McGraw[1], Thuc Nghi Nguyen[1], Julie Nyhus[1], Jeffrey G. Ojemann[8,10], Aaron Oldre[1], Sheana Parry[1], Shannon Reynolds[1], Christine Rimorin[1], Nadiya V. Shapovalova[1], Saroja Somasundaram[1], Aaron Szafer[1], Elliot R. Thomsen[1], Michael Tieu[1], Gerald Quon[2], Richard H. Scheuermann[5,11], Rafael Yuste[12], Susan M. Sunkin[1], Boudewijn Lelieveldt[3,4], David Feng[1], Lydia Ng[1], Amy Bernard[1], Michael Hawrylycz[1], John W. Phillips[1], Bosiljka Tasic[1], Hongkui Zeng[1], Allan R. Jones[1], Christof Koch[1] & Ed S. Lein[1]*

Elucidating the cellular architecture of the human cerebral cortex is central to understanding our cognitive abilities and susceptibility to disease. Here we used single-nucleus RNA-sequencing analysis to perform a comprehensive study of cell types in the middle temporal gyrus of human cortex. We identified a highly diverse set of excitatory and inhibitory neuron types that are mostly sparse, with excitatory types being less layer-restricted than expected. Comparison to similar mouse cortex single-cell RNA-sequencing datasets revealed a surprisingly well-conserved cellular architecture that enables matching of homologous types and predictions of properties of human cell types. Despite this general conservation, we also found extensive differences between homologous human and mouse cell types, including marked alterations in proportions, laminar distributions, gene expression and morphology. These species-specific features emphasize the importance of directly studying human brain.

The cerebral cortex is responsible for our higher cognitive abilities and is the most complex structure known to biology: it comprises 16 billion neurons and 61 billion non-neuronal cells organized into more than 100 distinct anatomical or functional regions[1,2]. Human cortex is expanded relative to mouse—the dominant model organism used in research—with a more-than-1,000-fold larger area and number of neurons[3]. Whereas the general principles of cortical development and basic architecture of the cortex appear to be conserved across mammals[4], previous studies suggest differences in the cellular makeup of human cortex[5–11]. For example, superficial cortical layers are expanded in mammalian evolution[12] and some cell types, such as interlaminar astrocytes[13] and rosehip neurons[14], have specialized features in human compared to mouse. Likewise, transcriptional regulation varies between mouse and human, including the transcription of genes that are associated with neuronal structure and function[15–17].

Single-cell transcriptomics enables molecular classification of cell types, provides a metric for comparative analyses, and is fuelling efforts to understand the complete cellular makeup of the mouse brain[18] and even the entire human body[19]. Single-cell RNA sequencing (scRNA-seq) of mouse cortex demonstrates robust transcriptional signatures of cell types[20–22] and suggests around 100 cell types per cortical area. Dissociating live cells from human brain is difficult, which makes scRNA-seq challenging to apply to this type of tissue, whereas single-nucleus RNA-seq (snRNA-seq) enables transcriptional profiling of nuclei from frozen human brain specimens[23,24]. Of note, nuclei contain sufficient gene-expression information to distinguish closely related cell types at a similar resolution to scRNA-seq[25,26], but early applications of snRNA-seq to human cortex did not have sufficient depth of coverage to achieve similar resolution to mouse studies[27,28]. Here, we established robust methods for the classification of cell types in human brain using snRNA-seq and compared cortical cell types to reveal conserved and divergent features of human and mouse cerebral cortex.

Transcriptomic taxonomy of cell types

To transcriptomically define cell types in human cortex, we used snRNA-seq and focused on middle temporal gyrus (MTG) largely from postmortem brain. MTG is often available from epilepsy resections, permitting comparison of postmortem versus live neurosurgical tissues, and enabling future correlation with in vitro slice physiology. Tissues were processed as described[14] (Fig. 1a, Extended Data Fig. 1a). Nuclei were collected from eight donor brains (Extended Data Table 1), with most coming from postmortem donors ($n = 15{,}206$) and a minority ($n = 722$) from layer (L)5 of MTG removed during neurosurgeries (Extended Data Fig. 2).

In total, 15,928 nuclei passed quality control, including those from 10,708 excitatory neurons, 4,297 inhibitory neurons and 923 non-neuronal cells. Nuclei from each broad class were iteratively clustered as described[26] (see Methods). Clusters were generally robust to different iterative clustering methods and were distinguished from nearest neighbours by at least 30 differentially expressed genes and at least one, and often more, binary markers. Requiring more binary markers led

[1]Allen Institute for Brain Science, Seattle, WA, USA. [2]Department of Molecular and Cellular Biology, University of California, Davis, Davis, CA, USA. [3]Department of Radiology, Leiden University Medical Center, Leiden, The Netherlands. [4]Department of Intelligent Systems, Delft University of Technology, Delft, The Netherlands. [5]J. Craig Venter Institute, La Jolla, CA, USA. [6]Department of Pathology, University of Washington, Seattle, WA, USA. [7]The Ben and Catherine Ivy Center for Advanced Brain Tumor Treatment, Swedish Neuroscience Institute, Seattle, WA, USA. [8]Department of Neurological Surgery, University of Washington School of Medicine, Seattle, WA, USA. [9]Epilepsy Surgery and Functional Neurosurgery, Swedish Neuroscience Institute, Seattle, WA, USA. [10]Regional Epilepsy Center at Harborview Medical Center, Seattle, WA, USA. [11]Department of Pathology, University of California, San Diego, San Diego, CA, USA. [12]Neurotechnology Center, Department of Biological Sciences, Columbia University, New York, NY, USA. [13]These authors contributed equally: Rebecca D. Hodge, Trygve E. Bakken. *e-mail: edl@alleninstitute.org

to the merging of some clusters (Extended Data Fig. 3). Marker genes for stringent clusters defined by four binary markers are provided in Supplementary Table 2. On average, neuronal nuclei were larger than non-neuronal nuclei, and median gene detection was higher for neurons (9,046 genes) than for non-neuronal cells (6,432 genes), as reported for mouse[21,22] (Extended Data Fig. 1). Transcriptomic cell types were largely conserved across individuals and tissue types, as all curated clusters contained nuclei from multiple donors, and nuclei from postmortem and neurosurgical tissues clustered together and had highly correlated expression within cell classes (Fig. 1b). Postmortem nuclei had slightly lower median gene detection than neurosurgical nuclei, and there was a small, consistent expression signature of tissue type. For example, neurosurgical nuclei had higher expression of some activity-regulated genes (for example, *FOS*), whereas postmortem nuclei had higher expression of ribosomal genes that correlate with postmortem interval[29] (Extended Data Fig. 2, Supplementary Table 1).

We defined 75 transcriptomically distinct cell types, including 45 inhibitory neuron types that express the GABAergic interneuron marker *GAD1*, 24 excitatory neuron types that express the vesicular glutamate transporter *SLC17A7* and 6 non-neuronal cell types that express the glutamate transporter *SLC1A3*. As expected[22], hierarchical relationships among types roughly mirror their developmental origins. We refer to clusters as cell 'types', intermediate order nodes as 'subclasses', higher order nodes (for example, interneurons from caudal ganglionic eminence (CGE)) as 'classes', and broad divisions (for example, excitatory neurons) as 'major classes'. Neurons split into two major classes: cortical plate-derived excitatory neurons and ganglionic eminence-derived inhibitory neurons. Non-neuronal types formed a separate branch based on differential expression of many genes (Fig. 1c). We developed a nomenclature for clusters on the basis of: (1) major cell class; (2) layer enrichment; (3) subclass marker gene; and (4) cluster-specific marker gene (Fig. 1c, Extended Data Fig. 4, Supplementary Table 2). We generated a searchable semantic representation of these clusters to link them to existing ontologies[30] (MTG ontology, Supplementary Table 3). We found broad correspondence to previous human cortex snRNA-seq studies[24,27,28], but identified many additional neuron types (Extended Data Fig. 5). Most cell types were rare (less than 0.7% of MTG neurons), including almost all interneuron types and deep-layer excitatory neuron types. However, upper-layer excitatory neurons were dominated by a small number of abundant types (more than 3.5% of MTG neurons). Excitatory types and many interneuron types were spatially restricted, whereas non-neuronal nuclei were distributed across all layers, with the notable exception of one astrocyte type (Fig. 1c).

Excitatory types often span layers

Excitatory neuron types broadly segregated by layer, expressed known laminar markers and were generally most similar to types in the same or adjacent layers (Fig. 2, Extended Data Fig. 6)—perhaps reflecting a developmental imprint of the inside-out generation of cortical layers[16]. Similarity by laminar proximity was also apparent in the hierarchical dendrogram structure except for excitatory L5–L6 neurons expressing *THEMIS* and *C1QL3* (Exc L5–L6 *THEMIS C1QL3*), which were transcriptionally similar to several L2–L3 and L5–L6 types. Exc L4–L5 *FEZF2 SCN4B* and Exc L4–L6 *FEZF2 IL26* were so distinct that they occupied separate branches on the dendrogram (Fig. 2a). Complex relationships between clusters are represented as constellation diagrams that capture both continuous and discrete variation in gene expression among types, as described[22] (Extended Data Fig. 6a).

Each excitatory type selectively expressed marker genes (Fig. 2b), although a combinatorial profile was often necessary to distinguish each type from all other types (Extended Data Fig. 7). Many of the markers have, to our knowledge, not been identified as such previously, and are important for cell function, such as basic helix–loop–helix (bHLH) transcription factors (*TWIST2*), collagens (*COL22A1*) and semaphorins (*SEMA3E*). Notably, 16 out of the 37 most-specific marker genes were unannotated or non-coding RNAs (ncRNAs). Cell-type-specific expression of ncRNAs is consistent with previous studies[31–33], could be validated in tissue sections and may have been detected here owing to preferential nuclear localization[32] or physical linkage of ncRNAs to chromatin[31] (Fig. 2b, Extended Data Fig. 8).

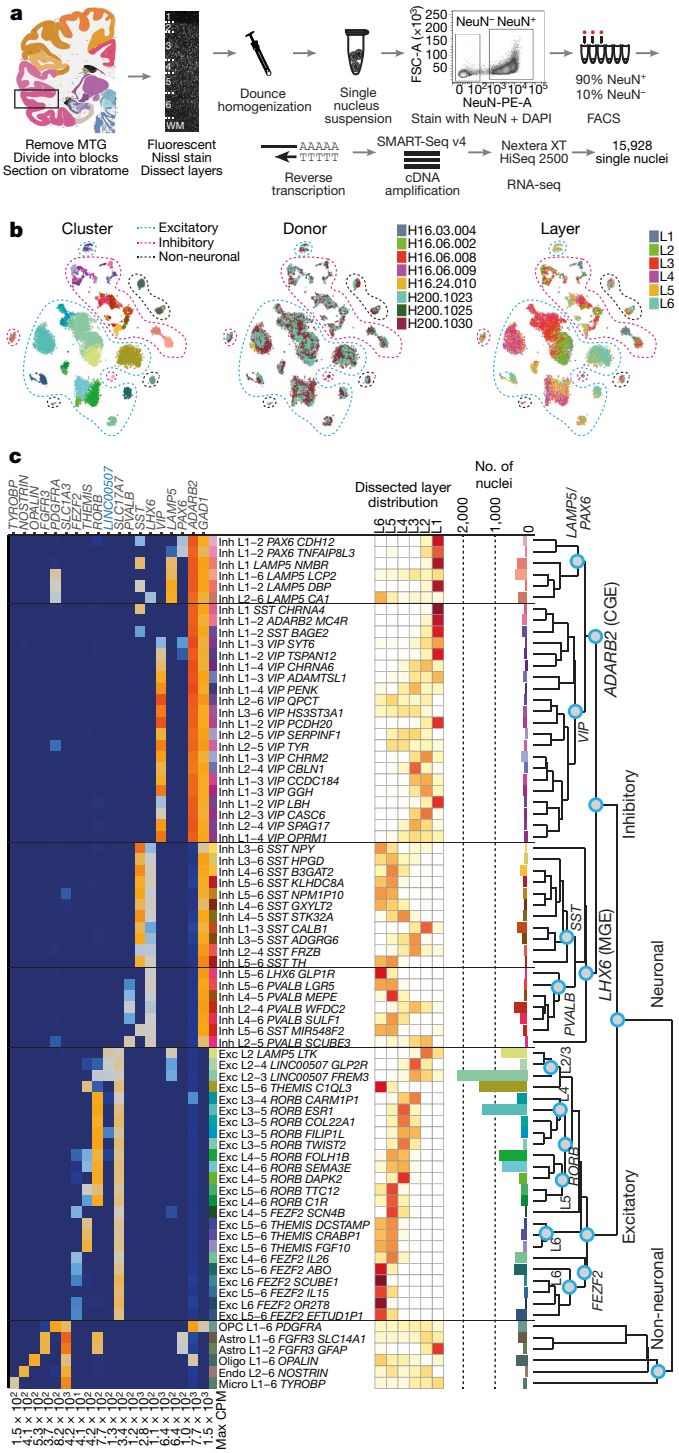

Fig. 1 | Cell-type taxonomy in human MTG. a, Schematic of RNA-sequencing analysis of neuronal (NeuN$^+$) and non-neuronal (NeuN$^-$) nuclei isolated from human MTG. Human brain image © 2010 Allen Institute for Brain Science. Allen Human Brain Atlas. Available from: http://human.brain-map.org/. **b**, *t*-distributed stochastic neighbour embedding (*t*-SNE) visualization of 15,928 nuclei grouped by expression similarity and coloured by cluster, donor and dissected layer. **c**, Taxonomy of 69 neuronal and 6 non-neuronal cell types based on median cluster expression. Branches are labelled with major cell classes. Cluster sizes, estimated laminar distributions (white, low; red, high) and median log-transformed expression of marker genes (blue, non-coding) across clusters are shown to the left. Maximum median gene expression (CPM, counts per million) is shown below.

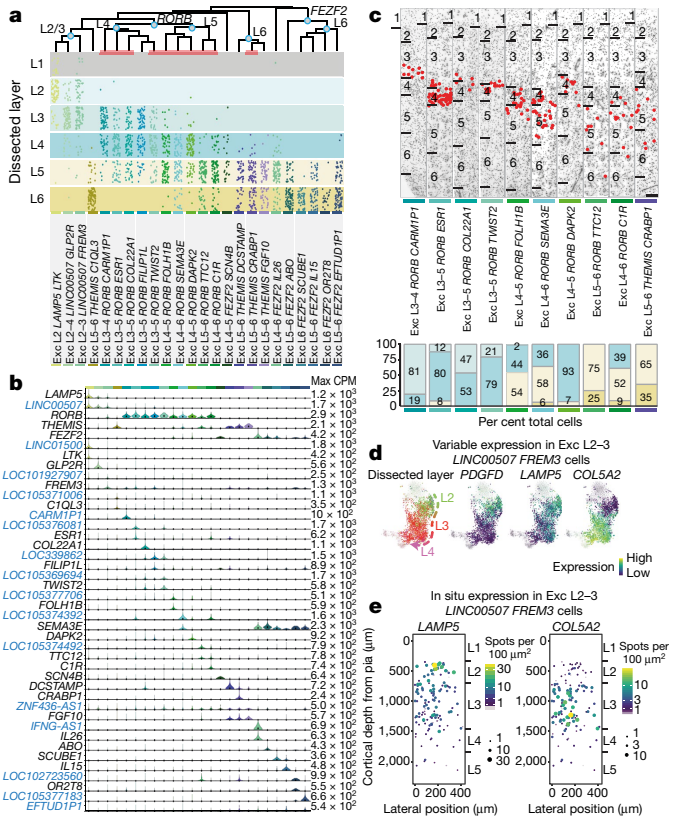

Fig. 2 | Excitatory neuron diversity and marker-gene expression. **a**, Estimated layer distributions of cell types based on dissected layer of nuclei (dots). L1 dissections included some excitatory neurons from L2. **b**, Violin plots of marker-gene (blue, non-coding) expression distributions across clusters ($n = 10{,}525$ nuclei). Rows represent genes, black dots represent median expression and maximum expression (CPM) is shown on the right. **c**, Representative inverted images of DAPI-stained cortical columns with cells (red dots) in each cluster (red bars in **a**) identified using marker genes listed in Extended Data Fig. 7. Experiments repeated on at least 2 donors per cell type. Scale bar, 250 μm. Bar plots summarize layer distributions for at least $n = 2$ donors per cell type. **d**, *t*-SNE maps of superficial excitatory neurons with nuclei in the Exc L2–3 *LINC00507 FREM3* cluster ($n = 2{,}284$) coloured by dissected layer and expression of *PDGFD*, *LAMP5* and *COL5A2*. **e**, smFISH quantification of *LAMP5* and *COL5A2* expression.

Unexpectedly, most excitatory neuron types were not restricted to dissections from single layers. Three types were enriched in L2–L3, ten *RORB*-expressing types were enriched in L3–L6, and four *THEMIS*-expressing and seven *FEZF2*-expressing types in L5–L6 (Fig. 2a, Extended Data Fig. 6a). Distribution across layers was not a result of dissection error; gene expression was consistent within each cluster across nuclei that were dissected from different layers (Extended Data Fig. 6b–e) and in situ distributions largely matched multilayer snRNA-seq predictions (Fig. 2a, c, Extended Data Fig. 7). Three types were localized to L3c and upper L4 (Fig. 2c). One (Exc L3–L4 *RORB CARM1P1*) had large nuclei (Extended Data Figs. 1b, 7), consistent with the giant pyramidal L3c neurons in MTG[34]. Two types were mostly in L4, but five others spanned multiple layers (Fig. 2c, Extended Data Fig. 7c). This heterogeneity implies that anatomical laminar location alone is insufficient to predict neuron type, although it remains to be seen whether this is a feature of MTG or human cortex generally.

Although upper layers are greatly expanded in human cortex relative to mouse, we still only found three main L2–L3 restricted excitatory types, just as in mouse cortex[22]. However, examination of Exc L2–L3 *LINC00507 FREM3* ($n = 2{,}284$ nuclei) revealed continuous gene-expression variation within this type (Fig. 2d, Supplementary Video 1), consistent with demonstrated diverse cellular properties in human L2–L3 excitatory neurons[34,35]. Fluorescence in situ hybridization (FISH) confirmed enrichment of *LAMP5* and *COL5A2* in L2 and L3 neurons, respectively, and Exc L2–L3 *LINC00507 FREM3* split into multiple subtypes with varying clustering parameters (Fig. 2e, Extended Data Figs. 3, 9). Thus, there is transcriptomic diversity within and between subtypes of L2–L3 excitatory neurons that probably corresponds to the anatomical and functional heterogeneity of these cells.

Inhibitory neuron diversity

Inhibitory neurons formed two major branches, distinguished by expression of *ADARB2* and *LHX6*—similar to mouse cortex, in which these branches correlate with developmental origins in CGE and medial ganglionic eminence (MGE), respectively[22]. The *LHX6* branch[36,37] included *PVALB* and *SST* subclasses and the *ADARB2* branch contained *LAMP5 PAX6* and *VIP* subclasses. Consistent with mouse, the *ADARB2* branch showed more diversity in L1–L3 than L4–L6, and the opposite was true for the *LHX6* branch (Fig. 3, Extended Data Fig. 10). As with excitatory neurons, many interneuron markers were ncRNAs (Fig. 3, Extended Data Fig. 4a). Surprisingly, the canonical mouse CGE interneuron marker *HTR3A*[38] was not expressed in human CGE types (Fig. 3c).

The *LAMP5 PAX6* subclass comprised six types mostly enriched in L1–L2 (Fig. 3a). Inhibitory (Inh) L1–L6 *LAMP5 LCP2* matched rosehip cells (Extended Data Fig. 5d), discovered in L1[14] but present in all cortical layers. Among *LAMP5 PAX6* types, only Inh L2–L6 *LAMP5 CA1* expressed *LHX6*, suggesting possible origins in MGE, similar to *Lamp5 Lhx6* cells described in mouse[22]. *VIP* was the most diverse subclass (21 types), with many types enriched in upper layers (Fig. 3a). Several *VIP* types were closely related to the *LAMP5 PAX6* type L1 *LAMP5 NMBR* and localized to L1–L2. Some CGE-derived cell types in L1 expressed *SST* (Fig. 3a, c), as described in human[14] but not in mouse L1 interneurons[22].

The *SST* subclass had 11 types that were spatially restricted, including the distinctive types Inh L5–L6 *SST TH* and Inh L3–L6 *SST NPY* in L5–L6 (Fig. 3b, d, Extended Data Fig. 10c). In situ hybridization showed sparse *TH* expression in L5–L6 of human MTG and the mouse homologous region (temporal association area (TEa)), suggesting that this gene marks similar cell types in both species, whereas *NPY* was much more sparsely expressed in human, indicating differential expression of this closely studied marker between species[39,40]. The *PVALB* subclass contained seven clusters; several *SST* and *PVALB* types were very similar (Fig. 3d, Extended Data Fig. 10b), pointing to close links between these subclasses. Inh L2–L5 *PVALB SCUBE3* is a distinctive type that expresses chandelier cell marker *UNC5B*[41] and probably corresponds to these specialized cells. Novel marker genes of this cluster label cells enriched in L2–L4 in situ (Fig. 3, Extended Data Fig. 10d).

Human MTG had similar proportions of MGE (44% *LHX6*$^+$ nuclei) and CGE (50% *ADARB2*$^+$ nuclei) interneurons on the basis of snRNA-seq data. By contrast, previous studies report around 70% MGE versus about 30% CGE interneurons in mouse cortex[38,42]. To further examine these differences, we quantified proportions of *ADARB2*$^+$ and *LHX6*$^+$ interneurons in human MTG and mouse TEa (Fig. 3e, Extended Data Fig. 10e, f). Interneurons co-expressing *ADARB2* and *LHX6* (Figs. 1, 3) were considered separately. Again, we found similar proportions of MGE (50.2 ± 2.3%, mean ± s.d.) and CGE (44.2 ± 2.4%) interneurons in human, and more than twice as many MGE (67.8 ± 0.9%) than CGE (30.8 ± 1.2%) interneurons in mouse. The increased proportion of CGE interneurons in human was greatest in L4 and the greatest decrease in MGE interneurons in human was in L4–L6 (Fig. 3e). snRNA-seq (6.1% of *GAD1*$^+$ cells) and cell counts (5.6 ± 0.3% of *GAD1*$^+$ cells) confirmed an increase in the proportion of *ADARB2* and *LHX6* co-expressing interneurons in human versus mouse (1.4 ± 0.2% of *GAD1*$^+$ cells), particularly in L6 (Fig. 3e).

Diverse morphology of astrocyte types

We identified major subclasses of non-neuronal cells, including two astrocyte types (Fig. 4). Astrocytes in human cortex are functionally[43]

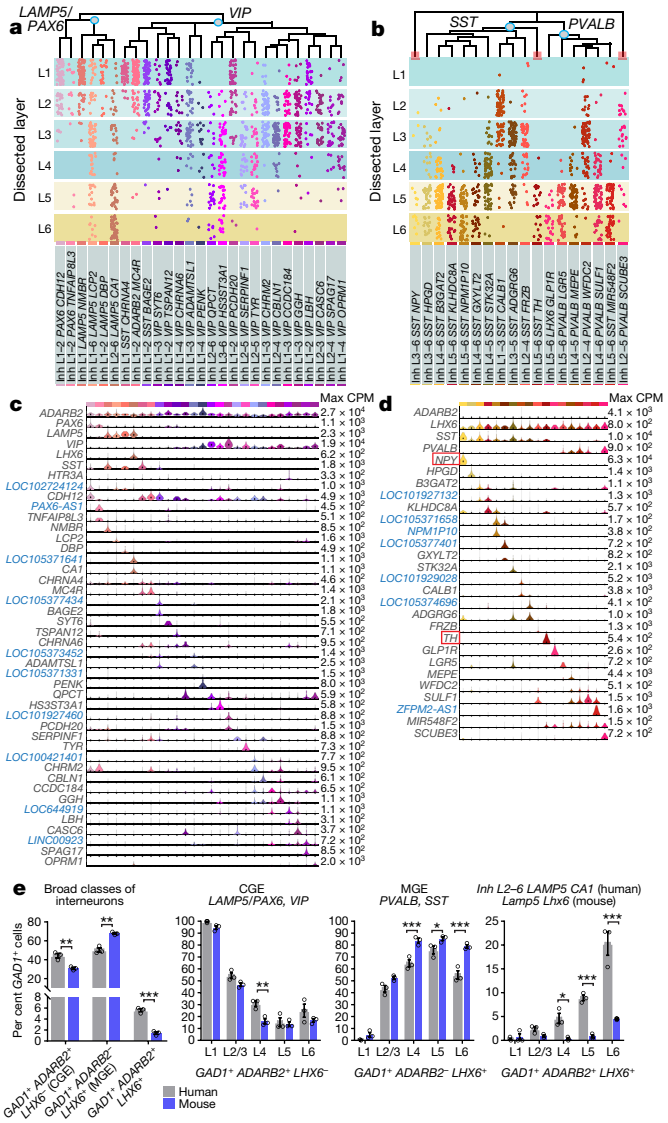

Fig. 3 | Inhibitory neuron diversity and layer distribution. a, **b**, Layer distributions of cell types estimated on the basis of dissected layer of nuclei ($n = 4{,}164$) (dots) and validated in situ for three clusters (red bars, Extended Data Fig. 10a, b). **c**, **d**, Violin plots of marker-gene (blue, non-coding) expression distributions across clusters (**c**; $n = 2{,}320$ nuclei; **d**; $n = 1{,}844$ nuclei). Rows represent genes, black dots show median expression and maximum expression (CPM) is shown on the right. **e**, Relative proportions and layer distributions of interneuron classes in human MTG and mouse TEa quantified by in situ labelling of marker genes with mFISH. Data are mean ± s.d. and circles represent individual specimens for human and mouse ($n = 3$). Two-tailed *t*-test with Holm–Sidak correction for multiple comparisons; degrees of freedom = 20; $^{*}P < 0.05$ $^{**}P < 0.01$, $^{***}P < 0.001$.

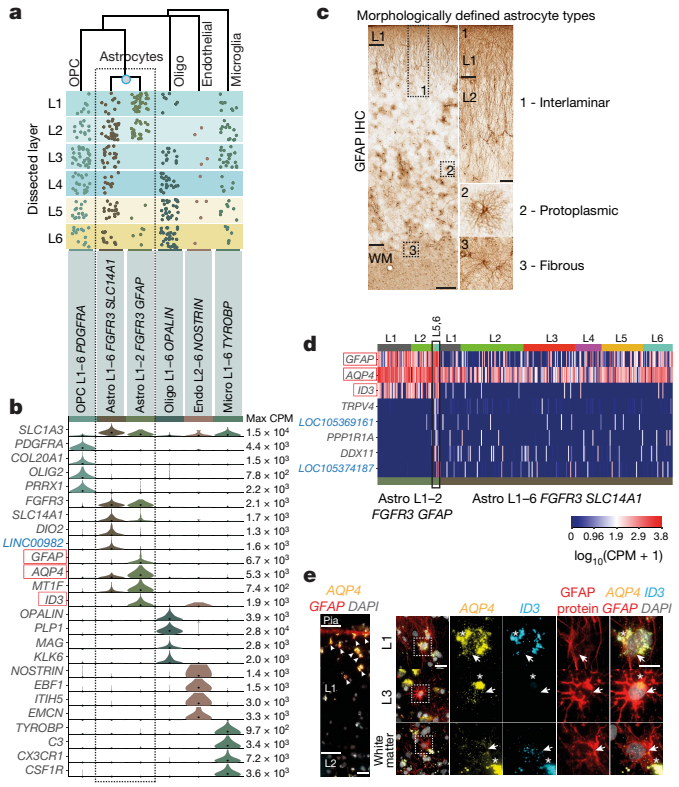

Fig. 4 | Non-neuronal cell-type diversity and marker-gene expression. a, Layer distributions of cell types estimated on the basis of dissected layer of nuclei (dots; $n = 914$). **b**, Violin plots of marker-gene (blue, non-coding) expression distributions across clusters. Rows represent genes, black dots show median expression and maximum expression (CPM) is shown on the far right. **c**, Immunohistochemistry (IHC) for GFAP shows morphologically defined human astrocyte types. Boxed regions are shown at higher magnification on the right. Scale bars, low magnification, 250 μm; high magnification, 50 μm. WM, white matter. **d**, Heat map of marker-gene expression with nuclei (columns) ordered by dissected layer. Several nuclei in deep layers (black box) express distinct markers. **e**, mFISH and immunohistochemistry of astrocyte subtype markers highlighted (red boxes) in **b**, **d**. Experiments repeated on $n = 2$ human donors. Left, cells with high expression of *AQP4* and *GFAP* in L1 (white arrowheads). Scale bar, 25 μm. Right top, cell in L1 co-expresses *AQP4* and *ID3* and has long GFAP-labelled processes. Right middle, protoplasmic astrocyte in L3 lacks expression of *ID3*. Right bottom, fibrous astrocyte at the white matter–L6 boundary expresses *AQP4*, *ID3* and GFAP protein. Asterisks mark lipofuscin. Boxed areas are magnified in the far right column. Scale bars, low magnification, 25 μm; high magnification, 15 μm.

and morphologically[13] specialized compared with rodent (Fig. 4c), with primate-specific interlaminar astrocytes residing in L1 and extending long processes, and protoplasmic astrocytes in L2–L6[13]. Indeed, we found two astrocyte types with different laminar distributions: Astrocyte (Astro) L1–L2 *FGFR3 GFAP* in L1–L2 and Astro L1–L6 *FGFR3 SLC14A1* in all layers (Fig. 4a). snRNA-seq showed that Astro L1–L2 *FGFR3 GFAP* expressed *ID3* and had higher *GFAP* and *AQP4* expression than Astro L1–L6 *FGFR3 SLC14A1* (Fig. 4b, d). Multiplex FISH (mFISH) for *GFAP* and *AQP4* showed cells with high expression of these genes in L1, and combined mFISH and GFAP immunohistochemistry showed cells in L1 that co-expressed *AQP4* and *ID3* and had long GFAP^{+} processes, consistent with interlaminar astrocytes. GFAP^{+} cells with protoplasmic astrocyte morphology lacked *ID3* expression, consistent with Astro L1–L6 *FGFR3 SLC14A1* (Fig. 4e). Whereas most nuclei in Astro L1–L2 *FGFR3 GFAP* came from L1–L2, seven were from L5–L6 dissections and expressed *ID3* and distinct markers. mFISH analysis showed that astrocytes co-expressing *ID3* and *AQP4* at the L6–white matter border had fibrous astrocyte morphology[13] (Fig. 4c–e). Therefore, we predict that sampling more non-neuronal nuclei will identify additional astrocyte diversity.

Human and mouse cell-type homology

To examine conservation of cellular architecture, we aligned transcriptomic cell types in human MTG to two distinct mouse cortical areas: primary visual cortex (V1) and a premotor area, the anterior lateral motor cortex (ALM)[22]. Matching cell types requires shared expression patterns between species, and we found that gene families (mean = 21 genes per set) that best discriminated mouse interneurons[41] also discriminated human interneurons (Fig. 5a). Similar genes also discriminated human and mouse excitatory types, but were less discriminating for non-neuronal cell types (Extended Data Fig. 11a).

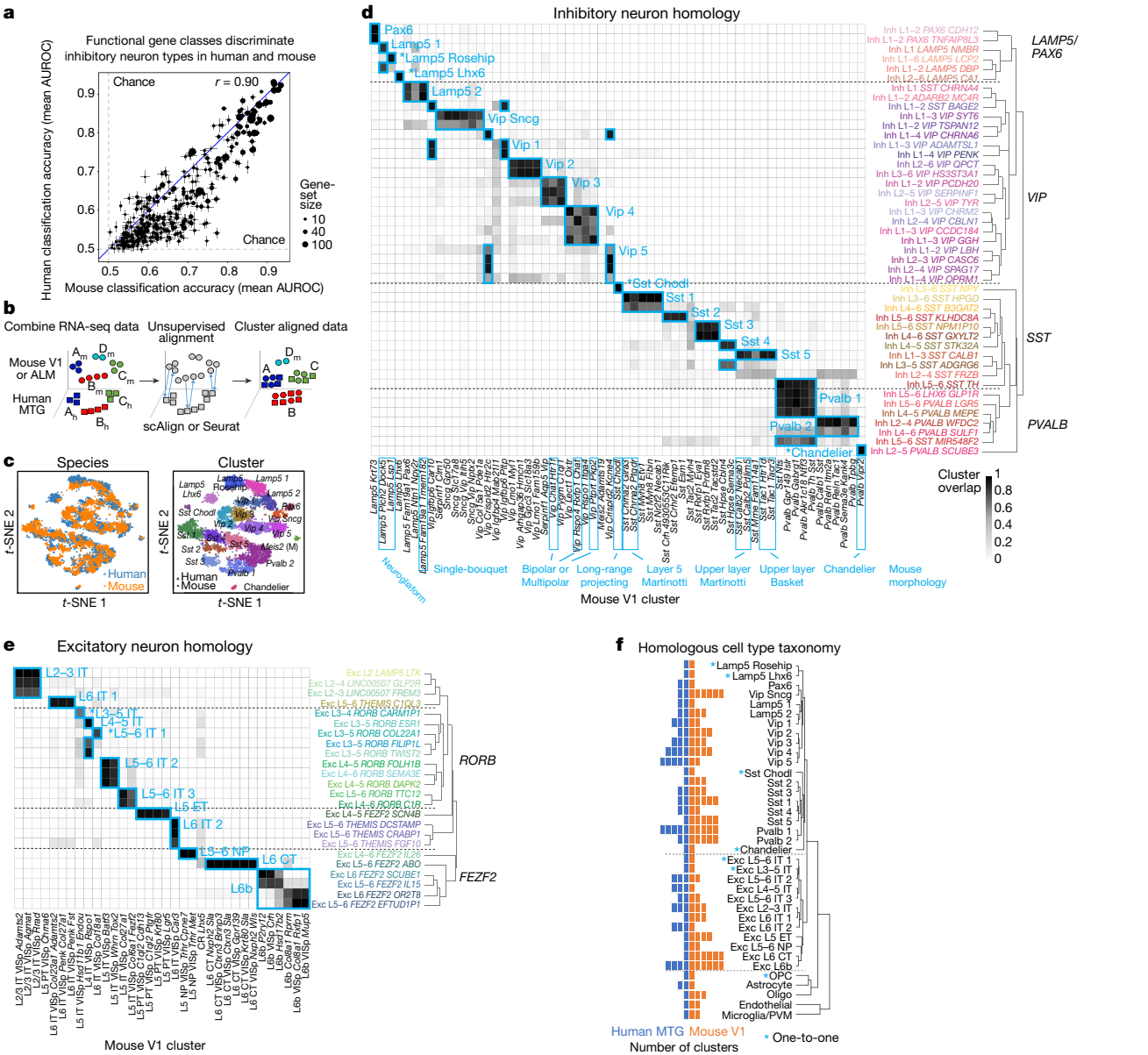

Fig. 5 | Evolutionary conservation of cell types between human and mouse. a, Similar functional gene families ($n = 384$ gene sets) discriminate inhibitory neuron types in human and mouse. Error bars correspond to the s.d. of mean MetaNeighbour AUROC scores across ten subsamples of cells. **b**, Schematic of unsupervised alignment and clustering of combined human (h) and mouse (m) cortical samples using scAlign or Seurat. **c**, *t*-SNE visualization of human ($n = 3{,}594$ nuclei) and mouse ($n = 6{,}595$ cells) inhibitory neuron clusters after alignment with scAlign. **d**, **e**, Human and mouse cell-type homologies for inhibitory neurons (**d**) and excitatory neurons from mouse V1 (**e**), predicted on the basis of shared cluster membership. Grey shade corresponds to the minimum proportion of human nuclei or mouse cells that co-cluster. Rows show human clusters and columns show mouse clusters. Homologous clusters are labelled on the basis of human and mouse cluster membership and include excitatory neuron projection targets (IT, intratelencephalic; ET, extratelencephalic–pyramidal tract; NP, near-projecting). Known morphologies indicated for mouse inhibitory types. VISp, primary visual cortex. **f**, Taxonomy of 32 neuronal and 5 non-neuronal homologous cell types and cell classes. Asterisks mark one-to-one matches. PVM, perivascular macrophages.

Applying principal component analysis (PCA) to combined expression data from inhibitory neurons from human MTG and mouse V1 separated samples first by species and then by cell type (Extended Data Fig. 11b). Applying canonical correlation analysis (CCA) based on shared co-expression patterns[44] and a neural network-based alignment algorithm (scAlign[45]) aligned human and mouse cortical samples that were then clustered. Homologous types were identified based on shared cluster membership (Fig. 5b–e, Extended Data Fig. 11d–f). Consistent cell-type homologies were obtained using a second alignment method based on dynamic time warping (Seurat) (Extended Data Fig. 11g, h) and by aligning human MTG to mouse V1 and ALM (Extended Data Fig. 12). These homologies were supported by shared marker genes between species (Extended Data Fig. 13, Supplementary Table 4). Clusters were combined into a hierarchical taxonomy of 32 neuronal and 5 non-neuronal cell types and subclasses (Fig. 5f). All major classes and subclasses were aligned and seven types were matched one-to-one between species.

Alignment of homologous types enabled prediction of cellular properties in human cortex. For example, Inh L2–L5 *PVALB SCUBE3* matched mouse chandelier cells (*Pvalb Vipr2*) and is predicted to selectively innervate axon initial segments of pyramidal neurons (Fig. 5d). Likewise, Inh L3–L6 *SST NPY* matched mouse *Sst Chodl* and is predicted to have long-range projections and contribute to sleep regulation[46]. Many other anatomically defined interneuron types could be inferred (Fig. 5d), although further experiments would be needed to test these predictions. Long-range projection targets of human

excitatory neurons could also be predicted. For example, Exc L4–L5 *FEZF2 SCN4B* cells matched mouse extratelencephalic-projecting (ET) L5 excitatory neurons (Fig. 5e) and are predicted to project subcortically. Of note, ET neurons are much less abundant in human than in mouse (1% versus 20% of L5 excitatory neurons)[22] (Extended Data Fig. 12e, f). Some homologous types shift layers between species, such as Exc L3–L4 *RORB CARM1P1* in L3 of human MTG, which matched L5-enriched types in mouse (Extended Data Fig. 12g).

Human non-neuronal cells matched a subset of mouse types (Extended Data Fig. 12c). Human oligodendrocytes matched two mouse mature oligodendrocyte types, whereas human oligodendrocyte precursor cells (OPCs) matched mouse one-to-one. Only nine endothelial cells were sampled in human and mapped to two endothelial subtypes in mouse. Both human astrocyte clusters mapped to one astrocyte cluster in mouse. Finally, human microglia clustered with mouse microglia and perivascular macrophages (Extended Data Fig. 11f).

Three rare mouse neuronal types lacked homologous human types. The mouse *Meis2* inhibitory type, primarily found in white matter[22], may have been missed owing to limited sampling of L6b white matter in human. Cajal–Retzius cells are very rare in adult human cortex (less than 0.1% of L1 neurons)[47] and were therefore unlikely to be sampled. Finally, mouse L5 pyramidal tract (PT) primary visual cortex *Chrna6*$^{+}$ cells, an ET type that projects to superior colliculus[48], aligned with only two human nuclei (Extended Data Fig. 11e), suggesting that a matching type may be found with deeper sampling in human.

Whereas many homologous subclasses had comparable diversity between species, some had expanded diversity in human and others were more diverse in mouse. For example, there was an apparent higher diversity of L4 excitatory neurons in human MTG than mouse V1. Mouse ET types were much more diverse than putative ET types in human, which may reflect either a species difference or likely undersampling, as they made up less than 1% of L5 excitatory neurons in MTG. L6 corticothalamic (CT) types were also more diverse in mouse V1 than human MTG. However, there were only two L6 CT types in mouse ALM, so this may reflect differences between primary sensory and association areas (Fig. 5e, f, Extended Data Fig. 12b, d).

Divergent cell-type expression between species

Identification of homologous types or classes enables analysis of conservation and divergence of gene-expression patterns across types. For each pair of homologous types, we compared expression of 14,553 orthologous genes between human and mouse (Fig. 6). Nuclear expression levels were estimated from intronic reads to better compare human snRNA-seq and mouse scRNA-seq data, as we previously found few differences in intronic expression between matched sets of mouse nuclei and whole cells[26] (Extended Data Fig. 11c). Comparison of homologous types showed a mix of conserved and divergent expression. The *Sst Chodl* type (Inh L3–L6 *SST NPY* in human) had conserved expression overall, but 18% of genes had highly divergent expression (defined conservatively here as a more-than-tenfold difference), including many marker genes. OPCs also had conserved expression and 14% highly divergent genes. Two thirds of all genes analysed (9,748) had divergent expression in at least one of 37 homologous types, and many had expression changes restricted to one type or class. Non-neuronal types had the most divergent expression (3,643 genes with more than tenfold difference), supporting increased evolutionary divergence of non-neuronal expression patterns between human and mouse[17] (Fig. 6a, b).

Most genes showed divergent expression only in a subset of types, resulting in a shift in the cell-type specificity of genes (quantified as the β-score, Methods, Supplementary Table 5). Genes with higher scores had high expression in at least one cell type and low expression in the remaining types, and were expressed in different subsets of types between species. Twenty-three per cent of genes (3,382) were more highly divergent than 95% of 252 housekeeping genes (Fig. 6c) recently shown to be stably expressed in multiple cell types in mouse and human[49]. Cell-type markers were less conserved than commonly

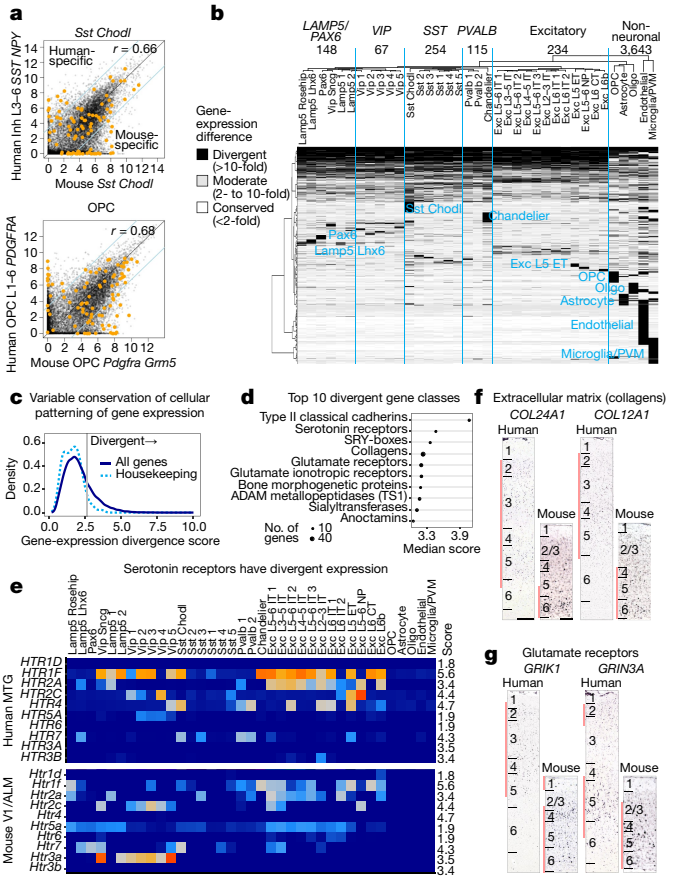

Fig. 6 | Divergent cell-type expression between human and mouse. **a**, Comparison of expression levels of 14,553 orthologous genes between human and mouse for *Sst Chodl* and OPCs. Genes outside the blue lines have highly divergent expression (>tenfold change) and include cluster-specific markers (orange dots). Pearson correlation (*r*). **b**, Patterns of expression change between human and mouse for 9,748 divergent genes (67% of orthologous genes). Groups of genes with similar patterns are labelled by the affected cell class. Top, number of genes with expression divergence restricted to each broad class of cell types. **c**, Distribution of scores (Methods) measuring the magnitude of expression change across homologous cell types for all genes (dark blue) and housekeeping genes (light blue). **d**, Gene families ($n > 10$ genes) with the most divergent expression patterns (highest score) include neurotransmitter receptors, ion channels and cell-adhesion molecules. **e**, Expression (trimmed average CPM) of most serotonin receptors differs between homologous cell types. Scores listed on far right. **f**, **g**, In situ hybridization of divergent genes shows shifts in laminar expression consistent with different cell-type expression in human and mouse. Red bars show layers with enriched expression. Scale bars, human, 250 μm; mouse, 100 μm.

expressed genes, and many markers were not shared between human and mouse. For example, chandelier cells express *Vipr2* in mouse but *COL15A1* and *NOG* in human (Extended Data Fig. 10d). Notably, the same gene families that show cell-type specificity in both species also show changed patterning across cell types (Figs. 5a, 6d, Supplementary Table 6).

Serotonin receptors exhibit highly divergent expression between species: four of seven G-protein-coupled receptors and both ionotropic receptor subunits (*HTR3A* and *HTR3B*) were in the top 10% most-divergent genes (Fig. 6e). The most-divergent gene families include neurotransmitter receptors, ion channels, extracellular matrix elements and cell-adhesion molecules. Among the top 3% most-divergent genes (Supplementary Table 5), the collagens *COL24A1* and *COL12A1* and glutamate receptor subunits *GRIK1* and *GRIN3A* were expressed in different cell types between species and were validated to have different laminar distributions in human and mouse (Fig. 6f, g). The cumulative effect of so many differences in the cellular patterning of genes

with well-characterized roles in neuronal signalling and connectivity is certain to cause many differences in human cortical circuit function.

Discussion

Single-cell transcriptomics enables systematic characterization of cellular diversity in the brain, allowing a paradigm shift in neuroscience from the historical emphasis on cellular anatomy to molecular classification of cell types. Echoing early anatomical studies[11], dense sampling of mouse cortex using scRNA-seq demonstrated great cellular diversity[21,22]. Here, similar dense sampling defined 75 cell types that represent non-neuronal (6), excitatory (24) and inhibitory (45) cells in human MTG. Notably, robust cell typing was achieved despite increased biological and technical variability between individual human brains. Importantly, these methods enabled the study of the cellular architecture of the human brain and the identification of homologous cell types to predict properties that cannot be directly measured in humans and generate hypotheses about conserved and divergent cell features.

Despite differences across datasets, alignment based on expression covariation reveals a cellular architecture that is largely conserved between cortical areas and species, as anatomical studies have shown for the last century. Here, mouse scRNA-seq was compared to human snRNA-seq; to mitigate this, expression levels were estimated using nuclear intronic sequence[26]. In addition, young adult transgenic mice were compared to genetically much more diverse older humans, but previous studies show stable gene expression in adulthood[50]. Finally, human MTG was compared with non-homologous mouse cortical areas. Although a matched analysis is preferable, primary visual cortex is specialized in human and likely to be highly divergent from mouse. Matching the human MTG taxonomy to mouse V1 and ALM taxonomies may seem at odds with the finding that excitatory neurons in mouse V1 and ALM cluster separately[22], but the magnitude of differential gene expression between cortical areas in mouse is small compared with that between species. Beyond similarities in overall diversity and hierarchical organization, most cell types mapped at the subclass level, seven cell types mapped one-to-one, and no major classes had missing homologous types despite the last common ancestor between humans and mice living at least 65 million years ago[51] and despite the thousand-fold difference in brain size and number of cells. Therefore, the transcriptomic organization of cell classes and subclasses appears conserved, with species and regional variation found at the finest level of cell-type distinction.

Our results demonstrate species divergence of gene expression between homologous cell types, as shown at the single-gene[15] and gross-structural level[16]. These differences are likely to be functionally relevant, as divergent genes are associated with connectivity and signalling, and many cell-type markers show divergent expression. Notably, serotonin receptors are the second-most-divergent gene family, challenging the use of mouse models for many neuropsychiatric disorders that involve serotonin signalling[52]. Homologous cell types can have highly divergent features in concert with divergent gene expression. For example, interlaminar astrocytes correspond to one of two human transcriptomic astrocyte types. Similarly, two astrocyte types were described in mouse cortex[21], including an L1 type that lacks the long processes of interlaminar astrocytes. Thus, a tenfold size increase and formation of long processes[13] are evolutionary variations on a conserved cell type. We observed several other evolutionary changes including differences in proportions of inhibitory neuron classes consistent with increased CGE generation of interneurons in human[36]. In addition, putative human L5 ET neurons are reduced in frequency (less than 1% in human versus approximately 20% in mouse), probably reflecting the 1,200-fold expansion of human cortex relative to mouse, compared with the only 60-fold expansion of the sub-cortical regions that these neurons target[2,3].

These observations quantitatively frame the debate of whether human cortex is different from that of other mammals[10,11], revealing basic transcriptomic similarity of cell types punctuated by differences in proportions and gene expression between species that are likely to influence microcircuit function. Furthermore, these results help to resolve the paradox of failures in the use of mouse for preclinical studies despite conserved structure across mammals[52,53], and highlight the need to analyse human brain in addition to model organisms. The magnitude of differences between human and mouse suggests similar profiling of closely related non-human primates is necessary to study many aspects of human brain structure and function. The enhanced resolution afforded by these molecular technologies also shows great promise for accelerating our mechanistic understanding of brain evolution and disease.

Online content

Any methods, additional references, Nature Research reporting summaries, source data, extended data, supplementary information, acknowledgements, peer review information; details of author contributions and competing interests; and statements of data and code availability are available at https://doi.org/10.1038/s41586-019-1506-7.

Received: 4 August 2018; Accepted: 17 July 2019;
Published online: 21 August 2019

1. Glasser, M. F. et al. A multi-modal parcellation of human cerebral cortex. *Nature* **536**, 171–178 (2016).
2. Azevedo, F. A. C. et al. Equal numbers of neuronal and nonneuronal cells make the human brain an isometrically scaled-up primate brain. *J. Comp. Neurol.* **513**, 532–541 (2009).
3. Herculano-Houzel, S., Mota, B. & Lent, R. Cellular scaling rules for rodent brains. *Proc. Natl Acad. Sci. USA* **103**, 12138–12143 (2006).
4. DeFelipe, J. The evolution of the brain, the human nature of cortical circuits, and intellectual creativity. *Front. Neuroanat.* **5**, 29 (2011).
5. Poorthuis, R. B. et al. Rapid neuromodulation of layer 1 interneurons in human neocortex. *Cell Rep.* **23**, 951–958 (2018).
6. Eyal, G. et al. Unique membrane properties and enhanced signal processing in human neocortical neurons. *eLife* **5**, e16553 (2016).
7. Szegedi, V. et al. Plasticity in single axon glutamatergic connection to GABAergic interneurons regulates complex events in the human neocortex. *PLoS Biol.* **14**, e2000237 (2016).
8. Benavides-Piccione, R., Ballesteros-Yáñez, I., DeFelipe, J. & Yuste, R. Cortical area and species differences in dendritic spine morphology. *J. Neurocytol.* **31**, 337–346 (2002).
9. Gabbott, P. L. Subpial fan cell—a class of calretinin neuron in layer 1 of adult monkey prefrontal cortex. *Front. Neuroanat.* **10**, 28 (2016).
10. Ramón y Cajal, S. *La Textura del Sistema Nerviosa del Hombre y los Vertebrados* (Nicolas Moya, 1904).
11. Lorente de Nó, R. La corteza cerebral del ratón. *Trab. Lab. Invest. Bio. (Madrid)* **20**, 41–78 (1922).
12. Hill, R. S. & Walsh, C. A. Molecular insights into human brain evolution. *Nature* **437**, 64–67 (2005).
13. Oberheim, N. A. et al. Uniquely hominid features of adult human astrocytes. *J. Neurosci.* **29**, 3276–3287 (2009).
14. Boldog, E. et al. Transcriptomic and morphophysiological evidence for a specialized human cortical GABAergic cell type. *Nat. Neurosci.* **21**, 1185–1195 (2018).
15. Zeng, H. et al. Large-scale cellular-resolution gene profiling in human neocortex reveals species-specific molecular signatures. *Cell* **149**, 483–496 (2012).
16. Bakken, T. E. et al. A comprehensive transcriptional map of primate brain development. *Nature* **535**, 367–375 (2016).
17. Hawrylycz, M. et al. Canonical genetic signatures of the adult human brain. *Nat. Neurosci.* **18**, 1832–1844 (2015).
18. Ecker, J. R. et al. The BRAIN initiative cell census consortium: lessons learned toward generating a comprehensive Brain Cell Atlas. *Neuron* **96**, 542–557 (2017).
19. Regev, A. et al. The Human Cell Atlas. *eLife* **6**, e27041 (2017).
20. Tasic, B. et al. Adult mouse cortical cell taxonomy revealed by single cell transcriptomics. *Nat. Neurosci.* **19**, 335–346 (2016).
21. Zeisel, A. et al. Brain structure. Cell types in the mouse cortex and hippocampus revealed by single-cell RNA-seq. *Science* **347**, 1138–1142 (2015).
22. Tasic, B. et al. Shared and distinct transcriptomic cell types across neocortical areas. *Nature* **563**, 72–78 (2018).
23. Krishnaswami, S. R. et al. Using single nuclei for RNA-seq to capture the transcriptome of postmortem neurons. *Nat. Protoc.* **11**, 499–524 (2016).
24. Lake, B. B. et al. Neuronal subtypes and diversity revealed by single-nucleus RNA sequencing of the human brain. *Science* **352**, 1586–1590 (2016).
25. Lake, B. B. et al. A comparative strategy for single-nucleus and single-cell transcriptomes confirms accuracy in predicted cell-type expression from nuclear RNA. *Sci. Rep.* **7**, 6031 (2017).
26. Bakken, T. E. et al. Single-nucleus and single-cell transcriptomes compared in matched cortical cell types. *PLoS ONE* **13**, e0209648 (2018).
27. Lake, B. B. et al. Integrative single-cell analysis of transcriptional and epigenetic states in the human adult brain. *Nat. Biotechnol.* **36**, 70–80 (2018).

28. Habib, N. et al. Massively parallel single-nucleus RNA-seq with DroNc-seq. *Nat. Methods* **14**, 955–958 (2017).
29. Zhu, Y., Wang, L., Yin, Y. & Yang, E. Systematic analysis of gene expression patterns associated with postmortem interval in human tissues. *Sci. Rep.* **7**, 5435 (2017).
30. Bakken, T. et al. Cell type discovery and representation in the era of high-content single cell phenotyping. *BMC Bioinformatics* **18**, 559 (2017).
31. Werner, M. S. et al. Chromatin-enriched lncRNAs can act as cell-type specific activators of proximal gene transcription. *Nat. Struct. Mol. Biol.* **24**, 596–603 (2017).
32. Derrien, T. et al. The GENCODE v7 catalog of human long noncoding RNAs: analysis of their gene structure, evolution, and expression. *Genome Res.* **22**, 1775–1789 (2012).
33. Liu, S. J. et al. Single-cell analysis of long non-coding RNAs in the developing human neocortex. *Genome Biol.* **17**, 67 (2016).
34. von Economo, C. *Cellular structure of the human cerebral cortex*. (Karger, 2009).
35. Kalmbach, B. E. et al. h-Channels contribute to divergent intrinsic membrane properties of supragranular pyramidal neurons in human versus mouse cerebral cortex. *Neuron* **100**, 1194–1208 (2018).
36. Hansen, D. V. et al. Non-epithelial stem cells and cortical interneuron production in the human ganglionic eminences. *Nat. Neurosci.* **16**, 1576–1587 (2013).
37. Ma, T. et al. Subcortical origins of human and monkey neocortical interneurons. *Nat. Neurosci.* **16**, 1588–1597 (2013).
38. Lee, S., Hjerling-Leffler, J., Zagha, E., Fishell, G. & Rudy, B. The largest group of superficial neocortical GABAergic interneurons expresses ionotropic serotonin receptors. *J. Neurosci.* **30**, 16796–16808 (2010).
39. Raghanti, M. A. et al. Neuropeptide Y-immunoreactive neurons in the cerebral cortex of humans and other haplorrhine primates. *Am. J. Primatol.* **75**, 415–424 (2013).
40. Xu, X., Roby, K. D. & Callaway, E. M. Immunochemical characterization of inhibitory mouse cortical neurons: three chemically distinct classes of inhibitory cells. *J. Comp. Neurol.* **518**, 389–404 (2010).
41. Paul, A. et al. Transcriptional architecture of synaptic communication delineates GABAergic neuron identity. *Cell* **171**, 522–539 (2017).
42. Miyoshi, G. et al. Genetic fate mapping reveals that the caudal ganglionic eminence produces a large and diverse population of superficial cortical interneurons. *J. Neurosci.* **30**, 1582–1594 (2010).
43. Zhang, Y. et al. Purification and characterization of progenitor and mature human astrocytes reveals transcriptional and functional differences with mouse. *Neuron* **89**, 37–53 (2016).
44. Butler, A., Hoffman, P., Smibert, P., Papalexi, E. & Satija, R. Integrating single-cell transcriptomic data across different conditions, technologies, and species. *Nat. Biotechnol.* **36**, 411–420 (2018).
45. Johansen, N. & Quon, G. scAlign: a tool for alignment, integration and rare cell identification from scRNA-seq data. *Genome Biol.* **20**, 166 (2019).
46. Kilduff, T. S., Cauli, B. & Gerashchenko, D. Activation of cortical interneurons during sleep: an anatomical link to homeostatic sleep regulation? *Trends Neurosci.* **34**, 10–19 (2011).
47. Belichenko, P. V., Vogt Weisenhorn, D. M., Myklóssy, J. & Celio, M. R. Calretinin-positive Cajal-Retzius cells persist in the adult human neocortex. *Neuroreport* **6**, 1869–1874 (1995).
48. Sorensen, S. A. et al. Correlated gene expression and target specificity demonstrate excitatory projection neuron diversity. *Cereb. Cortex* **25**, 433–449 (2015).
49. Lin, Y. et al. Evaluating stably expressed genes in single cells. Preprint at https://doi.org/10.1101/229815 (2018).
50. Colantuoni, C. et al. Temporal dynamics and genetic control of transcription in the human prefrontal cortex. *Nature* **478**, 519–523 (2011).
51. Foley, N. M., Springer, M. S. & Teeling, E. C. Mammal madness: is the mammal tree of life not yet resolved? *Phil. Trans. R. Soc. Lond. B* **371**, 20150140 (2016).
52. Markou, A., Chiamulera, C., Geyer, M. A., Tricklebank, M. & Steckler, T. Removing obstacles in neuroscience drug discovery: the future path for animal models. *Neuropsychopharmacology* **34**, 74–89 (2009).
53. Nestler, E. J. & Hyman, S. E. Animal models of neuropsychiatric disorders. *Nat. Neurosci.* **13**, 1161–1169 (2010).

METHODS

No statistical methods were used to predetermine sample size. The experiments were not randomized. The investigators were not blinded to allocation during experiments and outcome assessment.

Ethical compliance. De-identified postmortem human brain tissue was collected after obtaining permission from decedent next-of-kin. The Western Institutional Review Board (WIRB) reviewed the use of de-identified postmortem brain tissue for research purposes and determined that, in accordance with federal regulation 45 CFR 46 and associated guidance, the use of and generation of data from de-identified specimens from deceased individuals did not constitute human subjects research requiring institutional review board review. Postmortem tissue collection was performed in accordance with the provisions of the United States Uniform Anatomical Gift Act of 2006 described in the California Health and Safety Code section 7150 (effective 1/1/2008) and other applicable state and federal laws and regulations.

Tissue procurement from neurosurgical donors was performed outside of the supervision of the Allen Institute at local hospitals, and tissue was provided to the Allen Institute under the authority of the institutional review board of each participating hospital. A hospital-appointed case coordinator obtained informed consent from donors before surgery. Tissue specimens were de-identified before receipt by Allen Institute personnel. The specimens collected for this study were apparently non-pathological tissues removed during the normal course of surgery to access underlying pathological tissues. Tissue specimens collected were determined to be non-essential for diagnostic purposes by medical staff and would have otherwise been discarded.

All animal procedures were approved by the Institutional Animal Care and Use Committee at the Allen Institute for Brain Science (Protocol No. 1511). Mice were provided food and water ad libitum, maintained on a regular 12-h day/night cycle, and housed in cages with various enrichment materials added, including nesting materials, gnawing materials, and plastic shelters. Mice used in the study were adult (P56 $\pm$ 3 days) male and female wild-type C57Bl/6J animals.

Postmortem tissue donors. Males and females donors 18–68 years of age with no known history of neuropsychiatric or neurological conditions ('control' cases) were considered for inclusion in this study (Extended Data Table 1). Routine serological screening for infectious disease (HIV, Hepatitis B, and Hepatitis C) was conducted using donor blood samples and only donors negative for all three tests were considered for inclusion in the study. Tissue RNA quality was assessed using an Agilent Bioanalyzer-generated RNA Integrity Number (RIN) and Agilent Bioanalyzer electropherograms for 18S/28S ratios. Specimens with RIN values $\geq$ 7.0 were considered for inclusion in the study (Extended Data Table 1).

Processing of whole postmortem brain specimens. Whole postmortem brain specimens were transported to the Allen Institute on ice. Standard processing of whole brain specimens involved bisecting the brain through the midline and embedding of individual hemispheres in Cavex Impressional Alginate for slabbing. Coronal brain slabs were cut at 1cm intervals through each hemisphere and individual slabs were frozen in a slurry of dry ice and isopentane. Slabs were then vacuum sealed and stored at −80 °C until the time of further use.

MTG was identified on and removed from frozen slabs of interest, and subdivided into smaller blocks for further sectioning. Individual tissue blocks were processed by thawing in PBS supplemented with 10 mM DL-dithiothreitol (DTT, Sigma Aldrich), mounting on a vibratome (Leica), and sectioning at 500 μm in the coronal plane. Sections were placed in fluorescent Nissl staining solution (Neurotrace 500/525, ThermoFisher Scientific) prepared in PBS with 10 mM DTT and 0.5% RNasin Plus RNase inhibitor (Promega) and stained for 5 min on ice. After staining, sections were visualized on a fluorescence dissecting microscope (Leica) and cortical layers were individually microdissected using a needle blade micro-knife (Fine Science Tools).

Processing of neurosurgical tissue samples. Neurosurgical tissue was transported to the Allen Institute in chilled, oxygenated artificial cerebrospinal fluid (ACSF) consisting of the following: 0.5 mM calcium chloride (dehydrate), 25 mM D-glucose, 20 mM HEPES, 10 mM magnesium sulfate, 1.2 mM sodium phosphate monobasic monohydrate, 92 mM N-methyl-D-glucamine chloride (NMDG-Cl), 2.5 mM potassium chloride, 30 mM sodium bicarbonate, 5 mM sodium L-ascorbate, 3 mM sodium pyruvate, and 2 mM thiourea. The osmolality of the solution was 295-305 mOsm/kg and the pH was 7.3. Slices were prepared using a Compresstome VF-200 or VF-300 vibratome (Precisionary Instruments). After sectioning, slices were recovered in ACSF containing 2 mM calcium chloride (dehydrate), 25 mM D-glucose, 20 mM HEPES, 2 mM magnesium sulfate, 1.2 mM sodium phosphate monobasic monohydrate, 2.5 mM potassium chloride, 30 mM sodium bicarbonate, 92 mM sodium chloride, 5 mM sodium L-ascorbate, 3 mM sodium pyruvate, and 2 mM thiourea at room temperature for at least 1 h. After the recovery period, slices were transferred to RNase-free microcentrifuge tubes, snap frozen, and stored at −80 °C until the time of use. Microdissection of cortical layers was carried out on tissue slices that were thawed and stained as described above for postmortem tissue.

Nucleus sampling plan. Nuclei were sampled from 8 total human donors (4 male, 4 female; 4 postmortem, 4 neurosurgical; 24–66 years of age). To evenly survey cell-type diversity across cortical layers, nuclei were sampled based on relative proportions of neurons in each cortical layer[54]. We estimated that 16 cells were required to reliably discriminate two closely related Sst^+ interneuron types reported by Tasic et al.[20]. Monte Carlo simulations were used to estimate the sampling depth N needed to be 95% confident that at least 16 nuclei of frequency f have been selected from the population. Calculating N for a range of f revealed a simple linear approximation: $N = 28/f$. Subtypes of mouse cortical L5 projection neurons can be rarer than 1% of the population[48], so we targeted neuron types as rare as 0.2% of all cortical neurons. Based on Monte Carlo simulations, we estimated that 14,000 neuronal nuclei were needed to target types as rare as 0.2% of the total neuron population. Using an initial subset of RNA-seq data, we observed more transcriptomic diversity in L1, L5 and L6 than in other layers so additional neuronal nuclei (~1,000) were sampled from those layers. We also targeted 1,500 (10%) non-neuronal (NeuN-) nuclei and obtained approximately 1,000 nuclei that passed quality control (QC, see below), and we expected to capture types as rare as 3% of the non-neuronal population. Therefore, the final dataset contained <10% non-neuronal nuclei because nearly 50% of NeuN-negative nuclei failed QC, potentially due to the lower RNA content of glia compared to neurons[22].

Nucleus isolation and sorting. Microdissected tissue pieces were placed in into nuclei isolation medium containing 10mM Tris pH 8.0 (Ambion), 250mM sucrose, 25mM KCl (Ambion), 5mM MgCl2 (Ambion) 0.1% Triton-X 100 (Sigma Aldrich), 1% RNasin Plus, 1X protease inhibitor (Promega), and 0.1mM DTT in 1ml Dounce homogenizer (Wheaton). Tissue was homogenized using 10 strokes of the loose Dounce pestle followed by 10 strokes of the tight pestle and the resulting homogenate was passed through 30μm cell strainer (Miltenyi Biotech) and centrifuged at 900xg for 10 min to pellet nuclei. Nuclei were resuspended in buffer containing 1X PBS (Ambion), 0.8% nuclease-free BSA (Omni-Pur, EMD Millipore), and 0.5% RNasin Plus. Mouse anti-NeuN conjugated to PE (EMD Millipore) was added to preparations at a dilution of 1:500 and samples were incubated for 30 min at 4 °C. Control samples were incubated with mouse $IgG1_k$-PE Isotype control (BD Pharmingen). Samples were then centrifuged for 5 min at 400xg to pellet nuclei and pellets were resuspended in 1X PBS, 0.8% BSA, and 0.5% RNasin Plus. DAPI (4′, 6-diamidino-2-phenylindole, ThermoFisher Scientific) was applied to nuclei samples at a concentration of 0.1μg/ml.

Single nucleus sorting was carried out on either a BD FACSAria II SORP or BD FACSAria Fusion instrument (BD Biosciences) using a 130-μm nozzle. A standard gating strategy was applied to all samples. First, nuclei were gated on their size and scatter properties and then on DAPI signal. Doublet discrimination gates were used to exclude nuclei aggregates. Lastly, nuclei were gated on NeuN signal (PE). Ten percent of nuclei were intentionally sorted as NeuN-negative and the remaining 90% of nuclei were NeuN-positive. Single nuclei were sorted into 8-well strip tubes containing 11.5 μl of SMART-seq v4 collection buffer (Takara) supplemented with ERCC MIX1 spike-in synthetic RNAs at a final dilution of 1x10-8 (Ambion). Strip tubes containing sorted nuclei were briefly centrifuged and stored at −80 °C until the time of further processing. Index sorting was carried out for most samples to allow properties of nuclei detected during sorting to be connected with the cell-type identity revealed by subsequent snRNA-seq.

RNA-seq. We used the SMART-Seq v4 Ultra Low Input RNA Kit for Sequencing (Takara #634894) per the manufacturer's instructions for reverse transcription of RNA and subsequent cDNA amplification. Standard controls were processed alongside each batch of experimental samples. Control strips included: 2 wells without cells, 2 wells without cells or ERCCs (that is, no template controls), and either 4 wells of 10 pg of Human Universal Reference Total RNA (Takara 636538) or 2 wells of 10 pg of Human Universal Reference and 2 wells of 10 pg Control RNA provided in the Clontech kit. cDNA was amplified with 21 PCR cycles after the reverse transcription step. AMPure XP Bead (Beckman Coulter A63881) purification was done using an Agilent Bravo NGS Option A instrument with a bead ratio of 1x, and purified cDNA was eluted in 17 μl elution buffer provided by Takara. All samples were quantitated using PicoGreen (ThermoFisher Scientific) on a Molecular Dynamics M2 SpectraMax instrument. cDNA libraries were examined on either an Agilent Bioanalyzer 2100 using High Sensitivity DNA chips or an Advanced Analytics Fragment Analyzer (96) using the High Sensitivity NGS Fragment Analysis Kit (1 bp–6,000 bp). Purified cDNA was stored in 96-well plates at −20 °C until library preparation.

The NexteraXT DNA Library Preparation (Illumina FC-131-1096) kit with NexteraXT Index Kit V2 Sets A-D (FC-131-2001, 2002, 2003, or 2004) was used for sequencing library preparation. NexteraXT DNA Library prep was done at either 0.5x volume manually or 0.4x volume on the Mantis instrument (Formulatrix). Three different cDNA input amounts were used in generating the libraries: 75 pg, 100 pg, and 125 pg. AMPure XP bead purification was done using the Agilent Bravo NGS Option A instrument with a bead ratio of 0.9x and all samples were eluted in 22 μl of Resuspension Buffer (Illumina). Samples were quantitated using

PicoGreen on a Molecular Bynamics M2 SpectraMax instrument. Sequencing libraries were assessed using either an Agilent Bioanalyzer 2100 with High Sensitivity DNA chips or an Advanced Analytics Fragment Analyzer with the High Sensitivity NGS Fragment Analysis Kit for sizing. Molarity was calculated for each sample using average size as reported by Bioanalyzer or Fragment Analyzer and pg/μl concentration as determined by PicoGreen. Samples were normalized to 2–10 nM with Nuclease-free Water (Ambion). Libraries were multiplexed at 96 samples per lane and sequenced on an Illumina HiSeq 2500 instrument using Illumina High Output V4 chemistry. Libraries were sequenced at a median depth of 2.6 ± 0.5M reads/nucleus.

RNA-seq gene-expression quantification. Raw read (fastq) files were aligned to the GRCh38 human genome sequence (Genome Reference Consortium, 2011) with the RefSeq transcriptome version GRCh38.p2 (current as of 4/13/2015) and updated by removing duplicate Entrez gene entries from the gtf reference file for STAR processing. For alignment, Illumina sequencing adapters were clipped from the reads using the fastqMCF program[55]. After clipping, the paired-end reads were mapped using Spliced Transcripts Alignment to a Reference (STAR)[56] using default settings. STAR uses and builds it own suffix array index which considerably accelerates the alignment step while improving on sensitivity and specificity, due to its identification of alternative splice junctions. Reads that did not map to the genome were then aligned to synthetic constructs (that is, ERCC) sequences and the E.coli genome (version ASM584v2). The final results files included quantification of the mapped reads (raw exon and intron counts for the transcriptome-mapped reads). This quantification only includes uniquely mappable sequences, which makes up the vast majority of reads. A median of 88.4% of reads are uniquely mappable (range: 45.4–93.7%) compared with only 3.2% that are multi-mapping (range 1.6–10.1%), suggesting that any bias related to exclusion of multi-mappers would be relative minor. Also, part of the final results files are the percentages of reads mapped to the RefSeq transcriptome, to ERCC spike-in controls, and to *E. coli*, and summaries of these percentages are saved for quality control assessments. Quantification was performed using summerizeOverlaps from the R package GenomicAlignments[57]. Read alignments to the genome (exonic, intronic, and intergenic counts) were visualized as beeswarm plots using the R package beeswarm.

Expression levels were calculated as counts per million (CPM) of exonic plus intronic reads, and $\log_2(\text{CPM} + 1)$ transformed values were used for a subset of analyses as described below. Gene detection was calculated as the number of genes expressed in each sample with CPM > 0. CPM values reflected absolute transcript number and gene length, that is, short and abundant transcripts may have the same apparent expression level as long but rarer transcripts. Intron retention varied across genes so no reliable estimates of effective gene lengths were available for expression normalization. Instead, absolute expression levels were estimated as fragments per kilobase per million (FPKM) using only exonic reads so that annotated transcript lengths could be used.

Quality control of RNA-seq data. Nuclei were included for clustering analysis if they passed all of the following QC thresholds: >30% cDNA longer than 400 base pairs; >500,000 reads aligned to exonic or intronic sequence; >40% of total reads aligned; >50% unique reads; TA nucleotide ratio > 0.7.

After clustering (see below), clusters were identified as outliers if more than half of nuclei co-expressed markers of inhibitory (*GAD1, GAD2*) and excitatory (*SLC17A7*) neurons or were NeuN+ but did not express the pan-neuronal marker *SNAP25*. Median values of QC metrics listed above were calculated for each cluster and used to compute the median and inter-quartile range (IQR) of all cluster medians. Clusters were also identified as outliers if the cluster median QC metrics deviated by more than three times the IQRs from the median of all clusters. In total, 15,928 nuclei passed QC criteria and were split into three broad classes of cells (10,708 excitatory neurons, 4,297 inhibitory neurons, and 923 non-neuronal cells) based on NeuN staining and cell class marker-gene expression

Clusters were identified as donor-specific if they included fewer nuclei sampled from donors than expected by chance. For each cluster, the expected proportion of nuclei from each donor was calculated based on the laminar composition of the cluster and laminar sampling of the donor. For example, if 30% of L3 nuclei were sampled from a donor, then a L3-enriched cluster should contain approximately 30% of nuclei from this donor. In contrast, if only L5 were sampled from a donor, then the expected sampling from this donor for a L1-enriched cluster was zero. If the difference between the observed and expected sampling was greater than 50% of the number of nuclei in the cluster, then the cluster was flagged as donor-specific and excluded. In total, 325 nuclei were assigned to donor-specific or outlier clusters that contained marginal quality nuclei and were excluded from further analysis. Three donor-specific clusters came from neurosurgical donors ($n = 95$ nuclei) and were similar to other L5 types reported in our analysis, but had higher expression of activity-dependent genes.

To confirm exclusion, clusters automatically flagged as outliers or donor-specific were manually inspected for expression of broad cell class marker genes, mitochondrial genes related to quality, and known activity-dependent genes.

Clustering RNA-seq data. Nuclei and cells were grouped into transcriptomic cell types using an iterative clustering procedure based on community detection in a nearest neighbour graph as described in Bakken et al.[26]. In brief, intronic and exonic read counts were summed, and log2-transformed expression (CPM + 1) was centred and scaled across nuclei. X- and Y-chromosome were excluded to avoid nuclei clustering based on sex. Many mitochondrial genes had expression that was correlated with RNA-seq data quality, so nuclear and mitochondrial genes downloaded from Human MitoCarta2.0[58] were excluded. Differentially expressed genes were selected while accounting for gene dropouts, and PCA was used to reduce dimensionality. Nearest-neighbour distances between nuclei were calculated using up to 20 principal components, Jaccard similarity coefficients were computed, and Louvain community detection was used to cluster this graph with 15 nearest neighbours. Marker genes were defined for all cluster pairs using two criteria: 1) significant differential expression (> 2-fold; Benjamini–Hochberg false discovery rate < 0.01) using the R package limma and 2) binary expression (CPM > 1 in more than half of nuclei in one cluster and <30% of this proportion in the second cluster). Pairs of clusters were merged if either cluster lacked at least one marker gene. Clustering was then applied iteratively to each sub-cluster until the occurrence of one of four stop criteria: 1) fewer than six nuclei (due to a minimum cluster size of three), 2) no significantly variable genes, 3) no significantly variable PCs, 4) no significant clusters.

To assess the robustness of clusters, the iterative clustering procedure described above was repeated 100 times for random subsets of 80% of nuclei. A co-clustering matrix was generated that represented the proportion of clustering iterations that each pair of nuclei were assigned to the same cluster. We defined consensus clusters by iteratively splitting the co-clustering matrix as described in Tasic et al. 2018[22]. We used the co-clustering matrix as the similarity matrix and clustered using either Louvain (≥ 4,000 nuclei) or Ward's algorithm (<4,000 nuclei). We defined $N_{k,l}$ as the average probabilities of nuclei within cluster k to co-cluster with nuclei within cluster l. We merged clusters k and l if $N_{k,l} > \max(N_{k,k}, N_{l,l})$ - 0.25 or if the sum of $-\log_{10}$(adjusted P-value) of differentially expressed genes between clusters k and l was less than 150. Finally, we refined cluster membership by reassigning each nucleus to the cluster to which it had maximal average co-clustering. We repeated this process until cluster membership converged.

Next, we assessed the robustness of clusters using a similar clustering pipeline that was recently used to identify cortical cell types in mouse V1 and ALM[22]. This pipeline closely resembled the analysis described above except for three differences. First, this pipeline required that differentially expressed genes between all cluster pairs had more highly significant P values, and this penalized small clusters from splitting into sub-clusters. Second, the pipeline used Ward's agglomerative hierarchical clustering instead of Louvain community detection for iterations with fewer than 3,000 nuclei. Ward's method was computationally less efficient but improved detection of cluster heterogeneity when large and small clusters were present due to the well-known resolution of community detection algorithms that optimize global modularity[59]. Third, dimensionality reduction could be performed using WGCNA[60] rather than PCA, and this method was empirically more sensitive to subtle expression variation but also technical noise. This pipeline was run with four parameter settings, and the clustering results were compared to the reference clusters defined by the initial clustering pipeline. Confusion matrices were computed for each comparison and the Jaccard index was computed for all cluster pairs, and these results were summarized using box plots (Extended Data Fig. 3e).

The final set of clusters were compared to nearest neighbouring clusters and the number of differentially expressed genes (>2-fold change, Benjamini–Hochberg false discovery rate < 0.01) and binary marker genes (CPM > 1 in more the half of nuclei in one cluster and <30% of this proportion in the second cluster) were quantified and compared (Extended Data Fig. 3b) to the proportion of binary markers that were unannotated (that is, 'LOC' genes). If more markers were required to separate each cluster from its nearest neighbour, then clusters were merged and visualized as a river plot (Extended Data Fig. 3c). Clusters recently defined in mouse V1 and ALM required at least 4 binary markers (8 total markers with higher or lower expression than the nearest neighbouring cluster)[22]. 63 clusters in human MTG have at least 4 markers and are reported in Supplementary Table 2 along with markers selected as described below.

Cluster names were defined using an automated strategy which combined molecular information (marker genes) and anatomical information (layer of dissection). Clusters were assigned a broad class of interneuron, excitatory neuron, microglia, astrocyte, oligodendrocyte precursor, oligodendrocyte, or endothelial cell based on maximal median cluster CPM of *GAD1, SLC17A7, TYROBP, AQP4, PDGFRA, OPALIN* or *NOSTRIN*, respectively. Enriched layers were defined as the range of layers which contained at least 10% of the total cells from that cluster. Clusters were then assigned a broad marker, defined by maximal median CPM of *PAX6, LAMP5, VIP, SST, PVALB, LINC00507, RORB, THEMIS, FEZF2, TYROBP, FGFR3, PDGFRA, OPALIN* or *NOSTRIN*. Finally, clusters in all broad classes with more than one cluster (for example, interneuron, excitatory neuron, and astrocyte)

were assigned a gene showing the most-specific expression in that cluster (see details below). We developed a principled nomenclature for clusters based on: (1) major cell class, (2) layer enrichment (including layers containing at least 10% of nuclei in that cluster), (3) a subclass marker gene (maximal expression of 14 manually-curated genes), and (4) a cluster-specific marker gene (maximal detection difference compared to all other clusters). For example, the inhibitory neuron type at the top of the plot in Fig. 1c, found in samples dissected from L1 and L2, and expressing the subclass marker *PAX6* and the specific marker *CDH12*, is named Inh L1-2 *PAX CDH12*. A few cluster names were manually adjusted for clarity.

Marker-gene selection. *Scoring cluster marker genes.* Many genes were expressed in the majority of nuclei in a subset of clusters. A marker score (β) was defined for all genes to measure how binary expression was among clusters, independent of the number of clusters labelled (Supplementary Table 5). First, the proportion (x_i) of nuclei in each cluster that expressed a gene above background level (CPM >1) was calculated. Then, scores were defined as the squared differences in proportions normalized by the sum of absolute differences plus a small constant (ε) to avoid division by zero. Scores ranged from 0 to 1, and a perfectly binary marker had a score equal to 1.

$$\beta = \frac{\sum_{i=1}^{n}\sum_{j=1}^{n}(x_i - x_j)^2}{\sum_{i=1}^{n}\sum_{j=1}^{n}|x_i - x_j| + \varepsilon}$$

Specific cell-type marker genes. Specific marker genes were selected for cell-type naming and generation of violin plots and heat maps, and are included as part of Supplementary Table 2. For each cell type, the top marker genes were selected by filtering and sorting: first, only genes with highest proportion (CPM > 1) in the target cluster compared with every other cluster and with median expression at least twofold higher than in every other cluster were considered; and second, genes were filtered based on the difference in median expression in the top cluster compared with cluster with the next-highest median expression. The highest-ranked annotated gene (for example, not a 'LOC' or related gene) was selected as the specific gene to include in each cluster name. In clusters with no specific markers fold-change requirement was relaxed, and if still no marker was found then the most-specific gene compared with similar cell types (category level 3) was used (see Supplementary Table 2).

Combinatorial cell-type marker genes. Combinatorial marker genes were identified using NS-Forest v.2[61] (https://github.com/JCVenterInstitute/NSForest), an algorithm designed to select the minimum number of genes whose combined expression pattern is sufficient to uniquely classify cells of a particular type based on gene-expression clustering results. Briefly, for each gene-expression cluster, NS-Forest produces a random forest (RF) model for a target cluster vs all other clusters binary classification. The top-ranking genes (features) from each RF are then filtered by expression level (positive intermediate-high expression) and reranked by binary score. The binary score is calculated by first finding median cluster expression values for a given gene in each cluster. These values are then scaled by dividing by the median expression value in the target cluster. Next, we take one minus this scaled value such that the value will be 0 for the target cluster and 1 for clusters that have no expression (negative scaled values are set to 0). These values are then summed and normalized by dividing by the total number of clusters. In the ideal case, where all off-target clusters have no expression, the resulting binary score is 1. Finally, for the top 6 genes ranked by this binary score, optimal expression level cutoffs are determined using single decision trees, and all permutations of these genes are evaluated for classification accuracy using the $f-\beta$-score, where the β is weighted to favour precision. This *f* score indicates the power of discrimination for a cluster and a given set of genes. Top combinatorial markers are included as part of Supplementary Table 2.

Donor tissue-specific marker genes. Gene expression was compared between nuclei isolated from four neurosurgical and four postmortem donors. Differential expression analysis was performed with the limma R package using all NeuN-positive nuclei isolated from L5 of MTG. Donor sex and MTG cluster were included as covariates in a linear model, and all genes with at least a twofold difference in expression and Benjamini–Hochberg adjusted *P* value <0.05 are reported in Supplementary Table 1.

Cross-species marker genes. For each homologous cell type, cross-species markers were defined as having cluster-enriched expression (expressed in >50% of cells or nuclei in the cluster of interest and five or fewer additional clusters) in both species. Marker genes were rank ordered based on their cell type-specificity in human and mouse using a tau score defined in Yanai et al.[62]. Up to ten markers were plotted in Extended Data Fig. 11 and listed in Supplementary Table 4.

Assigning core and intermediate nuclei. We defined core and intermediate nuclei as described in[22]. Specifically, we used a nearest-centroid classifier, which assigns a nucleus to the cluster whose centroid has the highest Pearson's correlation with the nucleus. Here, the cluster centroid is defined as the median expression of the 1,200 marker genes with the highest β-score. To define core versus intermediate nuclei, we performed fivefold cross-validation 100 times. In each round, the nuclei were randomly partitioned into 5 groups, and nuclei in each group of 20% of the nuclei were classified by a nearest centroid classifier trained using the other 80% of the nuclei. A nucleus classified to the same cluster as its original cluster assignment more than 90 times was defined as a core nucleus, the others were designated intermediate nuclei. We define 14,204 core nuclei and 1,399 intermediate nuclei, which in most cases classify to only two clusters (1,345 out of 1,399, 96.1%). Most nuclei are defined as intermediate because they are confidently assigned to a different cluster from the one originally assigned (1,220 out of 1,399, 87.2%) rather than because they are not confidently assigned to any cluster.

Cluster dendrograms. Clusters were arranged by transcriptomic similarity based on hierarchical clustering. First, the average expression level of the top 1,200 marker genes (highest β-scores, as above) was calculated for each cluster. A correlation-based distance matrix ($D_{xy} = (1 - \rho(x, y))/2$) was calculated, and complete-linkage hierarchical clustering was performed using the hclust R function with default parameters. The resulting dendrogram branches were reordered to show inhibitory clusters followed by excitatory clusters, with larger clusters first, while retaining the tree structure. Note that this measure of cluster similarity is complementary to the co-clustering separation described above. For example, two clusters with similar gene-expression patterns but a few binary marker genes may be close on the tree but highly distinct based on co-clustering.

Organizing clusters into a provisional cell ontology. Annotations for gene-expression cluster characteristics were used to produce a provisional cell ontology representation as proposed[37], accessible through the BioPortal resource (https://bioportal.bioontology.org/ontologies/PCL) and an RDF representation available through a GitHub Repo (https://github.com/mkeshk2018/Provisional_Cell_Ontology). This ontology is presented in table form in Supplementary Table 3, along with more details about the components of this ontology.

Mapping cell types to reported clusters. 69 neuronal clusters in MTG were matched to 16 neuronal clusters reported by Lake et al.[24] using nearest-centroid classifier of expression signatures. Specifically, single nucleus expression data was downloaded for 3,042 cells and 25,051 genes. 1,359 marker genes (β-score >0.4) of MTG clusters that had a matching gene in the Lake et al. dataset were selected, and the median expression for these genes was calculated for all MTG clusters. Next, Pearson's correlations were calculated between each nucleus in the Lake et al. dataset and all 69 MTG clusters based on these 1,359 genes. Nuclei were assigned to the cluster with the maximum correlation. A confusion matrix was generated to compare the cluster membership of nuclei reported by Lake et al. and assigned MTG cluster. The proportion of nuclei in each MTG cluster that were members of each of the 16 Lake et al. clusters were visualized as a dot plot with circle sizes proportional to frequency and coloured by MTG cluster colour. The same comparative approach was performed for clusters defined using single nuclei isolated from prefrontal cortex, including 10,319 nuclei from Lake et al.[27] and 5,433 nuclei from Habib et al.[28].

Colorimetric in situ hybridization. In situ hybridization (ISH) data for human and mouse cortex was from the Allen Human Brain Atlas and Allen Mouse Brain Atlas. All ISH data are publicly accessible at https://www.brain-map.org. Data was generated using a semi-automated technology platform as described[63], with modifications for postmortem human tissues as previously described[15]. Digoxigenin-labelled riboprobes were generated for each human gene such that they would have >50% overlap with the orthologous mouse gene in the Allen Mouse Brain Atlas[63]. ISH experiments shown in Fig. 6 were repeated 4 (*COL24A1*), 3 (*COL12A1*, *GRIK1*), and 6 (*GRIN3A*) times for human, and 2 (*Col24a1*, *Col12a1*, *Grin3a*) and 6 (*Grik1*) times for mouse.

GFAP immunohistochemistry. Tissue slices (350 μm) from neurosurgical specimens were fixed for 2-4 days in 4% paraformaldehyde in PBS at 4 °C, washed in PBS and cryoprotected in 30% sucrose. Cryoprotected slices were frozen and re-sectioned at 30 μm using a sliding microtome (Leica SM2000R). Free floating sections were mounted onto gelatin coated slides and dried overnight at 37 °C. Slides were washed in 1X tris buffered saline (TBS), followed by incubation in 3% hydrogen peroxide in 1X TBS. Slides were then heated in sodium citrate (pH 6.0) for 20 min at 98 °C. After cooling, slides were rinsed in MilliQ water followed by 1X TBS. Primary antibody (mouse anti-GFAP, EMD Millipore, #MAB360, clone GA5, 1:1500) was diluted in Renaissance Background Reducing Diluent (Biocare #PD905L). Slides were processed using a Biocare intelliPATH FLX Automated Slide Stainer. After primary antibody incubation, slides were incubated in Mouse Secondary Reagent (Biocare #IPSC5001G20), rinsed with 1X TBS, incubated in Universal HRP Tertiary Reagent (Biocare #IPT5002G20), rinsed in 1X TBS, and incubated in IP FLXDAB (Biocare Buffer #IPBF5009G20), and DAB chromogen (Biocare Chromogen #IPC5008G3). Slides were then rinsed in 1X TBS, incubated in DAB sparkle (Biocare #DSB830M), washed in MilliQ water, dehydrated through a series of graded alcohols, cleared with Formula 83, and coverslipped with DPX. Slides were imaged using an Aperio ScanScope XT slide scanner (Leica).

Multiplex fluorescence in situ hybridization. Genes were selected for mFISH experiments that discriminated cell types and broader classes by visual inspection of differentially expressed genes that had relatively binary expression in the targeted types.

Single molecule FISH. Fresh-frozen human brain tissue from the MTG was sectioned at 10 μm onto Poly-L-lysine coated coverslips as described previously[64], let dry for 10 min at room temperature, then fixed for 15 min at 4 °C in 4% PFA. Sections were washed 3 × 10 min in PBS, then permeabilized and dehydrated with 100% isopropanol at room temperature for 3 min and allowed to dry. Sections were stored at −80 °C until use. Frozen sections were rehydrated in 2X SSC (Sigma Aldrich 20XSSC, 15557036) for 5 min, then treated 2 × 5 min with 4% SDS (Sigma Aldrich, 724255) and 200 mM boric acid (Sigma Aldrich, cat# B6768) pH 8.5 at room temperature. Sections were washed 3 times in 2X SSC, then once in TE pH 8 (Sigma Aldrich, 93283). Sections were heatshocked at 70 °C for 10 min in TE pH 8, followed by 2X SSC wash at room temperature. Sections were then incubated in hybridization buffer (10% Formamide (v/v, Sigma Aldrich 4650), 10% dextran sulfate (w/v, Sigma Aldrich D8906), 200 μg/mL BSA (Ambion AM2616), 2 mM ribonucleoside vanadyl complex (New England Biolabs, S1402S), 1 mg/ml tRNA (Sigma 10109541001) in 2X SSC) for 5 min at 38.5 °C. Probes were diluted in hybridization buffer at a concentration of 250 nM and hybridized at 38.5 °C for 2 h. Following hybridization, sections were washed 2 × 15 min at 38.5 °C in wash buffer (2X SSC, 20% Formamide), and 1 × 15 min in wash buffer with 5 μg/ml DAPI (Sigma Aldrich, 32670). Sections were then imaged in Imaging buffer (20 mM Tris-HCl pH 8, 50 mM NaCl, 0.8% glucose (Sigma Aldrich, G8270), 3 U/ml glucose oxidase (Sigma Aldrich, G2133), 90 U/ml catalase (Sigma Aldrich, C3515). Following imaging, sections were incubated 3 × 10 min in stripping buffer (65% formamide, 2X SSC) at 30 °C to remove hybridization probes from the first round. Sections were then washed in 2X SSC for 3 × 5 min at room temperature before repeating the hybridization procedure.

RNAscope mFISH. Human tissue specimens used for RNAscope mFISH came from a cohort of both neurosurgical or postmortem tissue donors that were independent from the donors used for snRNA-seq. Mouse tissue for RNAscope experiments was from adult (P56 +/− 3 days) male and female wild-type C57Bl/6J mice. Mice were anesthetized with 5% isoflurane and intracardially perfused with either 25 or 50 ml of ice cold, oxygenated artificial cerebral spinal fluid (0.5 mM $CaCl_2$, 25 mM D-Glucose, 98 mM HCl, 20 mM HEPES, 10 mM $MgSO_4$, 1.25 mM NaH_2PO_4, 3 mM Myo-inositol, 12 mM N-acetylcysteine, 96 mM N-methyl-D-glucamine, 2.5 mM KCl, 25 mM $NaHCO_3$, 5 mM sodium L-Ascorbate, 3 mM sodium pyruvate, 0.01 mM Taurine and 2 mM Thiourea). The brain was then rapidly dissected, embedded in optimal cutting temperature (OCT) medium, and frozen in a slurry of dry ice and ethanol. Tissues were stored at −80 °C for later cryosectioning.

Fresh-frozen mouse or human tissues were sectioned at 14–16 μm onto Superfrost Plus glass slides (Fisher Scientific). Sections were dried for 20 min at −20 °C and then vacuum sealed and stored at −80 °C until use. The RNAscope multiplex fluorescent v1 kit was used per the manufacturer's instructions for fresh-frozen tissue sections (Advanced Cell Diagnostics), with the following minor modifications: (1) fixation was performed for 60 min in 4% paraformaldehyde in 1X PBS at 4 °C, and (2) the protease treatment step was shortened to 10 min. Positive controls used to assess RNA quality in tissue sections were either from a set from Advanced Cell Diagnostics (*POLR2A*, *PPIB*, *UBC*, #320861) or a brain-specific probe combination (*SLC17A7*, *VIP*, *GFAP*). Sections were imaged using either a 40X or 60X oil immersion lens on a Nikon TiE fluorescent microscope equipped with NIS-Elements Advanced Research imaging software (version 4.20). For all RNAscope mFISH experiments, positive cells were called by manually counting RNA spots for each gene. Cells were called as positive for a gene if they contained ≥ 5 RNA spots for that gene. Lipofuscin autofluorescence was distinguished from RNA spot signal based on the larger size of lipofuscin granules and the broad fluorescence spectrum of lipofuscin.

RNAscope mFISH with GFAP immunohistochemistry. Tissue sections were processed for RNAscope mFISH detection of *ID3* (Advanced Cell Diagnostics, #492181-C3, NM_002167.4) and *AQP4* (Advanced Cell Diagnostics, #482441, NM_001650.5) exactly as described above. At the end of the RNAscope protocol, sections were fixed in 4% paraformaldehyde for 15 min at room temperature and then washed twice in 1X PBS for 5 min. Sections were incubated in blocking solution (10% normal donkey serum, 0.1% Triton-x 100 in 1X PBS) for 30 min at room temperature and then incubated in primary antibody diluted 1:100 in blocking solution (mouse anti-GFAP, Sigma-Aldrich, #G3893, clone G-A-5) for 18 h at 4C. Sections were then washed 3 times for 5 min each in 1X PBS, incubated with secondary antibody (goat anti-mouse IgG(H+L) Alexa Fluor 568 conjugate, ThermoFisher Scientific, #A-11004) for 30 min at room temperature, rinsed in 1X PBS 3 times for 5 min each, counterstained with DAPI (1 μg/ml), and mounted with ProLong Gold mounting medium (ThermoFisher Scientific). Sections were imaged using either a 40X or 60X oil immersion lens on a Nikon TiE fluorescent microscope equipped with NIS-Elements Advanced Research imaging software (version 4.20).

In situ validation of excitatory cell types and non-coding transcripts. To validate excitatory neuron types, clusters were labelled with cell-type-specific combinatorial gene panels using RNAscope mFISH. For each gene panel, positive cells were manually called by visual assessment of RNA spots for each gene, as described above. The total number of positive cells was quantified for each section. Positive cells were counted on at least three sections derived from at least two donors for each probe combination. DAPI staining was used to determine the boundaries of cortical layers within each tissue section and the laminar position of each positive cell was recorded. The percentage of labelled cells per layer, expressed as a fraction of the total number of labelled cells summed across all layers, was calculated for each type. Probes used were as follows (all from Advanced Cell Diagnostics): *SLC17A7* (#415611, NM_020309.3), *RORB* (#446061, #446061-C2, NM_006914.3), *CNR1* (#591521-C2, NM_001160226.1), *PRSS12* (#493931-C3, NM_003619.3), *ALCAM* (#415731-C2, NM_001243283.1), *MET* (#431021, NM_001127500.1), *MME* (#410891-C2, NM_007289.2), *NTNG1* (#446101-C3, NM_001113226.1), *HS3ST4* (#506181, NM_006040.2), *CUX2* (#425581-C3, NM_015267.3), *PCP4* (#446111, NM_006198.2), *GRIN3A* (#534841-C3, NM_133445.2), *GRIK3* (#493981, NM_000831.3), *CRHR2* (#469621, NM_001883.4), *TPBG* (#405481, NM_006670.4), *POSTN* (#409181-C3, NM_006475.2), *SMYD1* (#493951-C2, NM_001330364.1). Probes for non-coding transcripts were as follows (all from Advanced Cell Diagnostics): *LINC01164* (# 559051-C3, NR_038365.1), *LOC102723415* (#559031, XR_001741660.1), *LOC401134* (*LINC02232*, #559061-C3, NR_033976.1), *LOC105369818* (#508351-C3, XR_945055.2), *IFNG-AS1* (#508348-C2, NR_104124.1). *LOC105376081* (XR_929926.1) was assayed using colorimetric ISH as described above.

Imaging and quantification of smFISH expression. smFISH images were collected using an inverted microscope in an epifluorescence configuration (Zeiss Axio Observer.Z1) with a 63x oil immersion objective with numerical aperture 1.4. The sample was positioned in x, y and z with a motorized x, y stage with linear encoders and z piezo top-plate (Applied Scientific Instruments MS 2000-500) and z stacks with 300 nm plane spacing were collected in each colour at each stage position through the entire z depth of the sample. Fluorescence emission was filtered using a high-speed filterwheel (Zeiss) directly below the dichroic turret and imaged onto a sCMOS camera (Hamamatsu ORCA Flash4.0) with a final pixel size of 100 nm. Images were collected after each round of hybridization using the same configuration of x,y tile locations, aligned manually before each acquisition based on DAPI fluorescence. smFISH signal was observed as diffraction-limited spots which were localized in 3D image stacks by finding local maxima after spatial bandpass filtering. These maxima were filtered for total intensity and radius to eliminate dim background and large, bright lipofuscin granules. Outlines of cells and cortical layers were manually annotated on images of *GAD*, *SLC17A7* and DAPI as 2D polygons using FIJI. The number of mRNA molecules in each cell for each gene was then calculated and converted to densities (spots per 100 μm^2).

Background expression of the excitatory neuron marker *SLC17A7* was defined as the 95th quantile of *SLC17A7* spot density among cells in cortical L1, since no excitatory cells should be present in L1. Excitatory neurons were defined as any cell with *SLC17A7* spot density greater than this threshold. To map excitatory cells to MTG reference clusters, spot counts were log-transformed and scaled so that the 90th quantile of expression for each gene in smFISH matched the maximum median cluster expression of that gene among the reference clusters. Reference clusters that could not be discriminated based on the smFISH panel of nine genes were merged and all comparisons between smFISH and RNA-seq cluster classes were performed using these cluster groups. Scaled spot densities for each cell were then compared to median expression levels of each reference cluster using Pearson correlation, and each cell was assigned to the cluster with the highest correlation. For cells that mapped to the Exc L2-3 *LINC00507 FREM3* cluster, *LAMP5* and *COL5A2* expression was plotted as a dot plot where the size and colour of dots corresponded to probe spot density and the location corresponded to the *in situ* location.

In situ validation of putative chandelier cells. Tissue sections were labelled with the gene panel *GAD1, PVALB*, and *NOG*, or *COL15A1*, specific markers of the Inh L2-5 *PVALB SCUBE3* putative chandelier cell cluster. Probes were as follows (all from Advanced Cell Diagnostics): *GAD1* (#404031-C3, NM_000817.2), *PVALB* (#422181-C2, NM_002854.2), *NOG* (#416521, NM_005450.4), *COL15A1* (#484001, NM_001855.4). Counts were conducted on sections from 3 human tissue donors. For each donor, the total number of $GAD1^+$, $GAD1^+$, $PVALB^+$ and NOG^+ cells was summed across multiple sections. The laminar position of each cell, based on boundaries defined by assessing DAPI staining patterns in each tissue section, was recorded. The proportion of chandelier cells in each layer was calculated as a fraction of the total number of $GAD1^+PVALB^+NOG^+$ cells summed across all layers for each specimen.

Cell counts of broad interneuron classes. Tissue sections were labelled with the RNAscope Multiplex Fluorescent kit (Advanced Cell Diagnostics) as described above. For human tissue sections, the following probes (all from Advanced Cell Diagnostics) were used: *GAD1* (#404031, NM_000817.2); *ADARB2* (#511651-C3, NM_018702.3); *LHX6* (#460051-C2, NM_014368.4). For mouse tissue sections, the following probes were used: *Gad1* (#400951, NM_008077.4); *Adarb2* (#519971-C3, NM_052977.5); *Lhx6* (#422791-C2, NM_001083127.1). The expression of each gene was assessed by manual examination of corresponding RNA spots. Cell counts were conducted on sections from 3 human tissue donors: 2 neurosurgical and 1 postmortem. For mouse, 3 independent specimens were used. For both human and mouse, >500 total $GAD1^+$ cells per specimen were counted (Human, $n = 2{,}706$, 1,553, and 3,476 $GAD1^+$ cells per donor, respectively; Mouse, $n = 1{,}897$, 2,587, and 708 $GAD1^+$ cells per specimen, resepectively). Expression of *ADARB2/Adarb2* and *LHX6/Lhx6* was manually assessed in each $GAD1^+$ cell and cells were scored as being positive ($\geq$5 RNA spots/gene) or negative for each gene, as described above. At the same time, the laminar position of each $GAD1^+$ cell was recorded. Cell density, highlighted by DAPI staining, was used to determine laminar boundaries. The percentage of each cell class expressed as a fraction of total $GAD1^+$ cells and the percentage of each cell class per layer, expressed as a fraction of the total number of $GAD1^+$ cells per layer, were calculated for each specimen. Statistical comparisons between human and mouse were done using unpaired two-tailed *t*-tests with Holm–Sidak correction for multiple comparisons.

MetaNeighbour analysis. To compare the ability of different gene families to distinguish cell types in mouse versus human cortex, we performed a modified supervised MetaNeighbour analysis[65] independently for both species. First, we divided our datasets into two artificial experiments, selecting random groups of equal size up to a maximum of 10 cells per cluster for each experiment. We next ran MetaNeighbour separately for clusters from each broad class (GABAergic, glutamatergic, and non-neuronal) using the R function run_MetaNeighbor where experiment_labels are 1 or 2 corresponding to the two artificial experiments, cell-type_labels are 2 for cells in the targeted cluster and 1 for cells in all other clusters of the same broad class, and genesets were all of the HGNC gene sets included in supplementary table 3 of ref. [41]. Mean AUROC scores for each gene set were then calculated by averaging the reported AUROC scores for a gene set across all clusters within a given broad class. This processes was repeated for 10 divisions of the human and mouse data into random experimental groups. Means and standard deviations of these mean AUROC scores for human and mouse GABAergic cell types are compared in Fig. 5.

Estimation of cell-type homology. We aligned single nucleus and single cell RNA-seq data from human MTG and either mouse primary visual cortex (V1) or ALM cortex by applying two data integration methods, Seurat[44] and scAlign[45], to remove species-specific differences. As a secondary analysis, we aligned mouse V1 to mouse ALM excitatory neurons using the same analysis pipeline.

First, we quantified expression levels as $\log_2$-transformed CPM of intronic plus exonic reads. Including exonic reads increased experimental differences due to measuring whole cell (mouse) versus nuclear (human) transcripts, but this was out-weighed by improved gene detection. We separated each dataset into three broad cell classes: GABAergic, glutamatergic, and non-neuronal, based on their assigned clusters, and selected up to 200 cells from each cluster. For excitatory neurons from ALM, we selected up to 50 cells from each cluster to improve the alignment of rare types. For each species comparison, we selected the union of the top 2,000 genes with the highest dispersion for human and mouse and calculated up to 40 canonical correlates with diagonal CCA. We used these canonical correlates as input to scAlign's encoder neural network or Seurat's dynamic time warping algorithm[44].

In brief, scAlign is a neural network that learns a mapping from the canonical correlation space of data from each species into a common cell state space in which functionally similar cells occupy the same region of the cell state space. The neural network optimizes a loss function which encourages overlap of similar cells across species while preserving cell-cell similarity within each species to minimize the species-specific distortion in the learned cell state space. The default network architecture for scAlign is defined by: Input (CCA) → FC(512) → FC(256) → FC(128) → FC(32). The input nodes consist of the single cell transcriptome profiles that have been preprocessed via canonical correlation analysis. Here, FC(n) defines a fully connected layer with *n* hidden units and a ReLU activation function. The final FC(n) layer outputs the cell embeddings. Following each FC(n) layer, we used batch normalization and dropout at a rate of 30%. Key hyperparameters for scAlign were set as follows. (1) Mini-batch size ranged between 100 and 1,000 cells to ensure sufficient representation of each cell type to avoid bias. (2) Perplexity values of 5, 10, and 30 defined the number of neighbours for each cell. (3) Weight of L2 regularization in the loss function was set to 0.0001. (4) Learning rate was initialized at 0.0001 and followed a linear decay pattern during training. (5) The number of FC(n) layers varied from 2 to 4 as larger FC(n) layers were consecutively removed. All training converged in less than 15,000 iterations.

To identify the optimal model architecture(s) for each experiment, we measured two quality metrics defined on scAlign's cell embeddings: (1) accuracy of a 5-nearest neighbours classifier for labelling human and mouse cells and (2) alignment score[44] measuring the degree of mixing between human and mouse cells. These scores were averaged across three random weight initializations to validate that the model produced robust alignments. We also tested the robustness of the alignment to different methods by using nonlinear warping implemented in the Seurat R package for alignment.

We defined homologous cell types by clustering the aligned embedding output from scAlign or Seurat and identifying human and mouse samples that co-clustered. First, a weighted graph was constructed based on the Jaccard similarity of the nearest neighbours of each sample. Louvain community detection was run to identify clusters that optimized the global modularity of the partitioned graph. For each pair of human and mouse clusters, the overlap was defined as the sum of the minimum proportion of samples in each cluster that overlapped within each CCA cluster. This approach identified pairs of human and mouse clusters that consistently co-clustered within one or more aligned clusters. Cluster overlaps varied from 0 to 1 and were visualized as a heat map with human MTG clusters in rows and mouse V1 or ALM clusters in columns.

Cell-type homologies were identified as one-to-one, one-to-many, or many-to-many based on the pattern of overlap between clusters. Including more canonical correlates or fewer nearest neighbours increased the number of cell types that could be discriminated within each species but also reduced alignment between species and resulted in more species-specific clusters. A grid based search was used to select the optimal number of canonical correlates (30, inhibitory neurons; 40, excitatory neurons; 10, non-neuronal) and nearest neighbours that maximized detection of homologous cell types. Most homologies were consistent between MTG and two mouse cortical areas (V1 and ALM) and between alignment methods, although scAlign gave somewhat higher resolution homologies (Extended Data Fig. 9). Inconsistencies between cell-type homologies in MTG and V1 or ALM were resolved by grouping clusters to identify a coarser homology. For example, all L6b clusters in human and mouse were assigned to a single L6b homologous type. Supplementary Table 3 lists homologies defined using scAlign between MTG and V1 for all clusters and between MTG and ALM for excitatory neuron clusters. Homologous type names were assigned based on the annotations of member clusters from human and mouse.

Quantification of expression divergence. For each pair of 37 homologous human and mouse cell types, the average expression of 14,553 orthologous genes was calculated as the average counts per million of intronic reads. Only intronic reads were used to better compare these single nucleus (human) and single cell (mouse) datasets. Average expression values were log2-transformed and scatter plots and Pearson's correlations were calculated to compare human and mouse. Genes were ranked based on their cell type-specificity in human and mouse using a tau score defined in Yanai et al.[62], and the union of the top 50 markers in human and mouse were highlighted in the scatter plots. The fold difference in expression between human and mouse was calculated for all genes and homologous cell types and thresholded to identify large (>10-fold), moderate (2 to tenfold), and small (<2-fold) differences. A heat map was generated showing expression differences across cell types, and hierarchical clustering using Ward's method was applied to group genes with similar patterns of expression change. For each of 6 major classes of cell types (*LAMP5/PAX6*, *VIP*, *SST*, *PVALB*, excitatory, non-neuronal), the number of genes was quantified that had >10-fold change in at least one cell type in that class and <10-fold change in all cell types in the other 5 classes. The expression pattern change of 14,553 genes was quantified as the β-score (see marker score methods above) of $\log_2$-expression differences across 37 homologous cell types (Supplementary Table 2). Scores ranged from 0–1 and measured the magnitude of expression changes between species while normalizing for the number of cell types that changed expression. Genes with high scores have a large fold change in expression in one or more (but not all) cell types. For each gene, the number of clusters with median expression (CPM) > 1 was compared to the median pattern change of those genes. A loess curve and standard error were fit using the R package ggplot. Finally, the median pattern change was calculated for functional gene families downloaded from the HUGO Gene Nomenclature Committee (HGNC) at https://www.genenames.org/download/statistics-and-files/.

Reporting summary. Further information on research design is available in the Nature Research Reporting Summary linked to this paper.

Data availability

Data can be accessed through the Allen Brain Atlas data portal at http://portal.brain-map.org/ and RNA-seq data from this study are publicly available and can be downloaded at http://celltypes.brain-map.org/. Data can be visualized and analysed using two complementary viewers: the RNA-seq Data Navigator (http://celltypes.brain-map.org/rnaseq/human) and the Cytosplore Viewer (https://viewer.cytosplore.org/), an extension of Cytosplore[66] that presents a hierarchy of *t*-SNE maps

of different subsets of MTG clusters[67]. An ontology of cell types can be navigated at http://bioportal.bioontology.org/ontologies/PCL. Controlled access raw RNA-seq data are registered with dbGAP (accession number phs001790) and have been deposited at the NeMO archive (https://nemoarchive.org/). Applications to access raw sequencing data should be submitted via dbGAP.

Code availability

The data and code used to produce figures are available from https://github.com/AllenInstitute/MTG_celltypes.

54. DeFelipe, J., Alonso-Nanclares, L. & Arellano, J. I. Microstructure of the neocortex: comparative aspects. *J. Neurocytol.* **31**, 299–316 (2002).
55. Aronesty, E. Comparison of sequencing utility programs. *Open Bioinform. J.* **7**, 1–8 (2013).
56. Dobin, A. et al. STAR: ultrafast universal RNA-seq aligner. *Bioinformatics* **29**, 15–21 (2013).
57. Lawrence, M. et al. Software for computing and annotating genomic ranges. *PLOS Comput. Biol.* **9**, e1003118 (2013).
58. Calvo, S. E., Clauser, K. R. & Mootha, V. K. MitoCarta2.0: an updated inventory of mammalian mitochondrial proteins. *Nucleic Acids Res.* **44**, D1251–D1257 (2016).
59. Fortunato, S. & Barthélemy, M. Resolution limit in community detection. *Proc. Natl Acad. Sci. USA* **104**, 36–41 (2007).
60. Langfelder, P. & Horvath, S. WGCNA: an R package for weighted correlation network analysis. *BMC Bioinformatics* **9**, 559 (2008).
61. Aevermann, B. D. et al. Cell type discovery using single-cell transcriptomics: implications for ontological representation. *Hum. Mol. Genet.* **27**, R40–R47 (2018).
62. Yanai, I. et al. Genome-wide midrange transcription profiles reveal expression level relationships in human tissue specification. *Bioinformatics* **21**, 650–659 (2005).
63. Lein, E. S. et al. Genome-wide atlas of gene expression in the adult mouse brain. *Nature* **445**, 168–176 (2007).
64. Lyubimova, A. et al. Single-molecule mRNA detection and counting in mammalian tissue. *Nat. Protocols* **8**, 1743–1758 (2013).
65. Crow, M., Paul, A., Ballouz, S., Huang, Z. J. & Gillis, J. Characterizing the replicability of cell types defined by single cell RNA-sequencing data using MetaNeighbor. *Nat. Commun.* **9**, 884 (2018).
66. Höllt, T. et al. Cytosplore: Interactive immune cell phenotyping for large single-cell datasets. *Comput. Graph. Forum* **35**, 171–180 (2016).
67. Höllt, T. et al. CyteGuide: Visual guidance for hierarchical single-cell analysis. *IEEE Trans. Vis. Comput. Graph.* **24**, 739–748 (2018).

Acknowledgements We thank the Tissue Procurement, Tissue Processing and Facilities teams at the Allen Institute for Brain Science for assistance with the transport and processing of postmortem and neurosurgical brain specimens; the Technology team at the Allen Institute for assistance with data management; our collaborators at the Swedish Medical Center and Harborview Medical Center in Seattle for coordinating human neurosurgical tissue collections; M. Vawter, J. Davis and the San Diego Medical Examiner's Office for assistance with postmortem tissue donations; and the Molecular Biology, Histology and Imaging teams at the Allen Institute for Brain Science for performing chromogenic in situ hybridization experiments. A. M. Yanny provided technical assistance with RNAscope experiments. This work was funded by the Allen Institute for Brain Science and by US National Institutes of Health grant U01 MH114812-02 to E.S.L. Funding from NWO-AES projects 12721: Genes in Space and 12720: VANPIR (principal investigator A. Vilanova) for development of the Cytosplore Viewer is gratefully acknowledged. We thank B. van Lew for scripting and narration of Cytosplore instructional and use-case videos. Support for the development of NS-Forest v.2 and the provisional cell ontology was provided by the Chan–Zuckerberg Initiative DAF, an advised fund of the Silicon Valley Community Foundation (2018-182730). G.Q. is supported by NSF CAREER award 1846559. This publication is part of the Human Cell Atlas (https://www.humancellatlas.org/publications). The authors thank the Allen Institute founder, Paul G. Allen, for his vision, encouragement and support.

Author contributions E.S.L. conceptualized and supervised the study. E.S.L. and R.Y. conceptualized the Human Cell Types Program. R.D.H. and T.E.B. designed experiments. R.D.H., E.R.B., B. Long., J.L.C., B.P.L., S.I.S., K.B., J.G., D.H., S.-L.D., M.M., S.P., E.R.T., N.V.S., E.G., T.N.N. and Z.M. contributed to nuclei isolation and/or validation experiments. T.E.B. and J.A.M. analysed the data with contributions from N.J., O.P., Z.Y., O.F., J.G., S.S., G.Q. and M.H. K.A.S. and B.T. managed the snRNA-seq pipeline. L.T.G. developed data visualization tools. D.B., K.L., C.R. and M.T. performed snRNA-seq. A. Bernard and J.W.P. managed establishment of the snRNA-seq pipeline. A. Bernard and M.M. contributed to the development and management of histological methods and data generation. R.D., N.D., T.C., J.N. and A.O. processed postmortem brain tissues. A. Bernard and N.D. managed acquisition of postmortem and neurosurgical tissues. A. Beller, C.D.K., C.C., R.G.E., R.P.G., A.L.K. and J.G.O. contributed to neurosurgical tissue collections. B.A., M.K. and R.H.S. developed the semantic representation of clusters. J.E., T.H., A.M. and B. Lelieveldt developed the Cytosplore Viewer. L.T.G., J.A.M., D.F., L.N. and A. Bernard contributed to the development of the RNA-Seq Data Navigator. S.R., A.S. and S.M.S. provided programme management and/or regulatory compliance support. C.K. and A.R.J. provided institutional support and project oversight. E.S.L. and H.Z. directed the Allen Institute Cell Types Program. R.D.H., T.E.B. and E.S.L. wrote the paper with contributions from J.A.M. and J.L.C. and in consultation with all authors.

Competing interests The authors declare no competing interests.

Additional information

Supplementary information is available for this paper at https://doi.org/10.1038/s41586-019-1506-7.

Correspondence and requests for materials should be addressed to E.S.L.

Peer review information *Nature* thanks Thomas Mrsic-Flogel, Rahul Satija and the other, anonymous, reviewer(s) for their contribution to the peer review of this work.

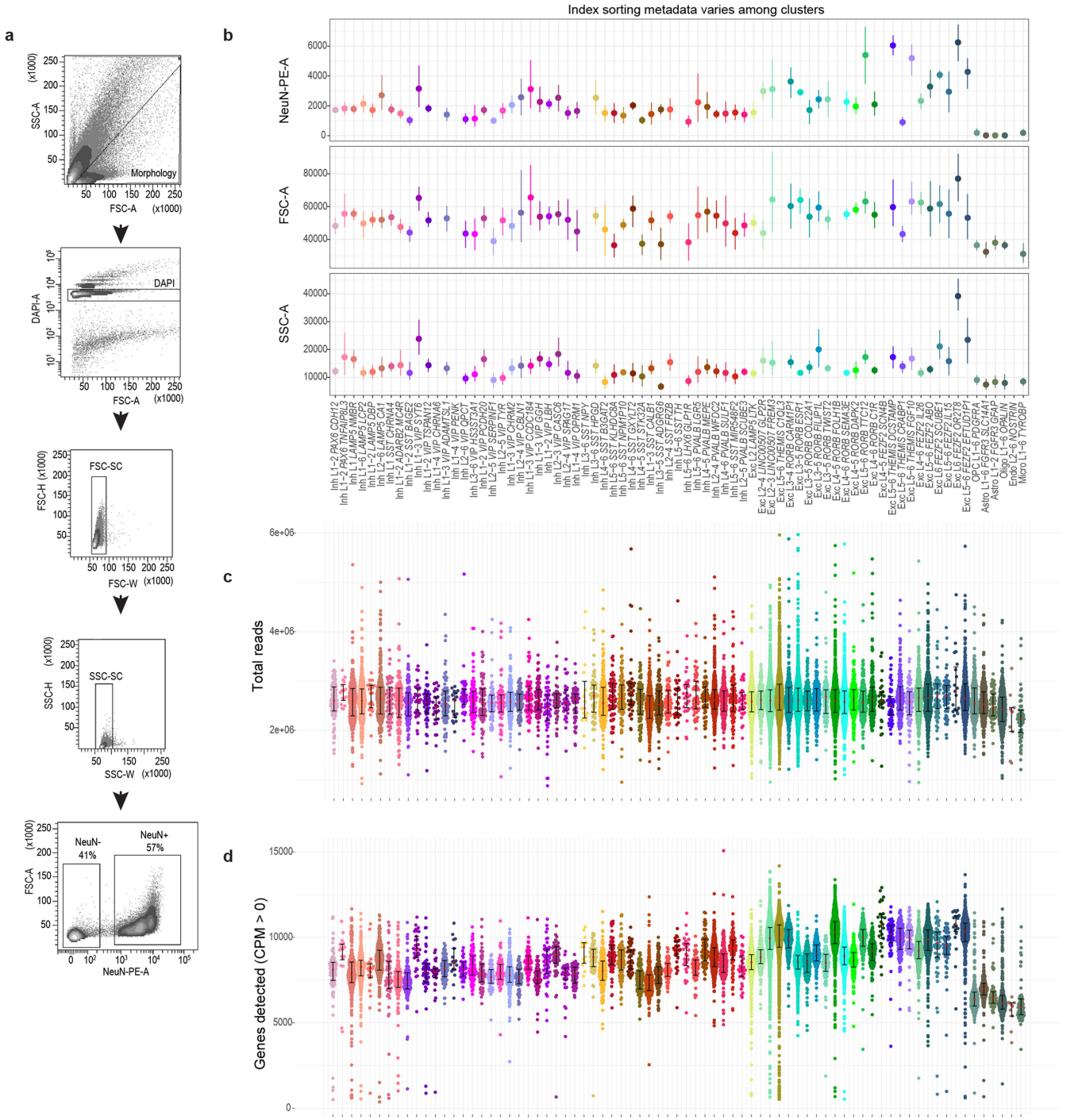

Extended Data Fig. 1 | Nuclei metadata summarized by cluster. a, FACS gating scheme for nuclei sorts. **b**, FACS metadata for index-sorted single nuclei ($n = 571$) show significant variability in NeuN fluorescence intensity (NeuN–PE-A), size (forward-scatter area, FSC-A) and granularity (side-scatter area, SSC-A) across clusters. As expected, non-neuronal nuclei have almost no NeuN staining and are smaller (as inferred by lower FSC values). Error bars represent 95% bootstrapped confidence intervals on mean values (points). **c, d**, Scatter plots of single nuclei from all clusters ($n = 15{,}928$) plus median and interquartile interval of three quality control metrics grouped and coloured by cluster. **c**, Median total reads were approximately 2.6 million for all cell types, although slightly lower for non-neuronal nuclei. **d**, Median gene detection was highest among excitatory neuron types in L5 and L6 and a subset of types in L3, lower among inhibitory neuron types and significantly lower among non-neuronal types.

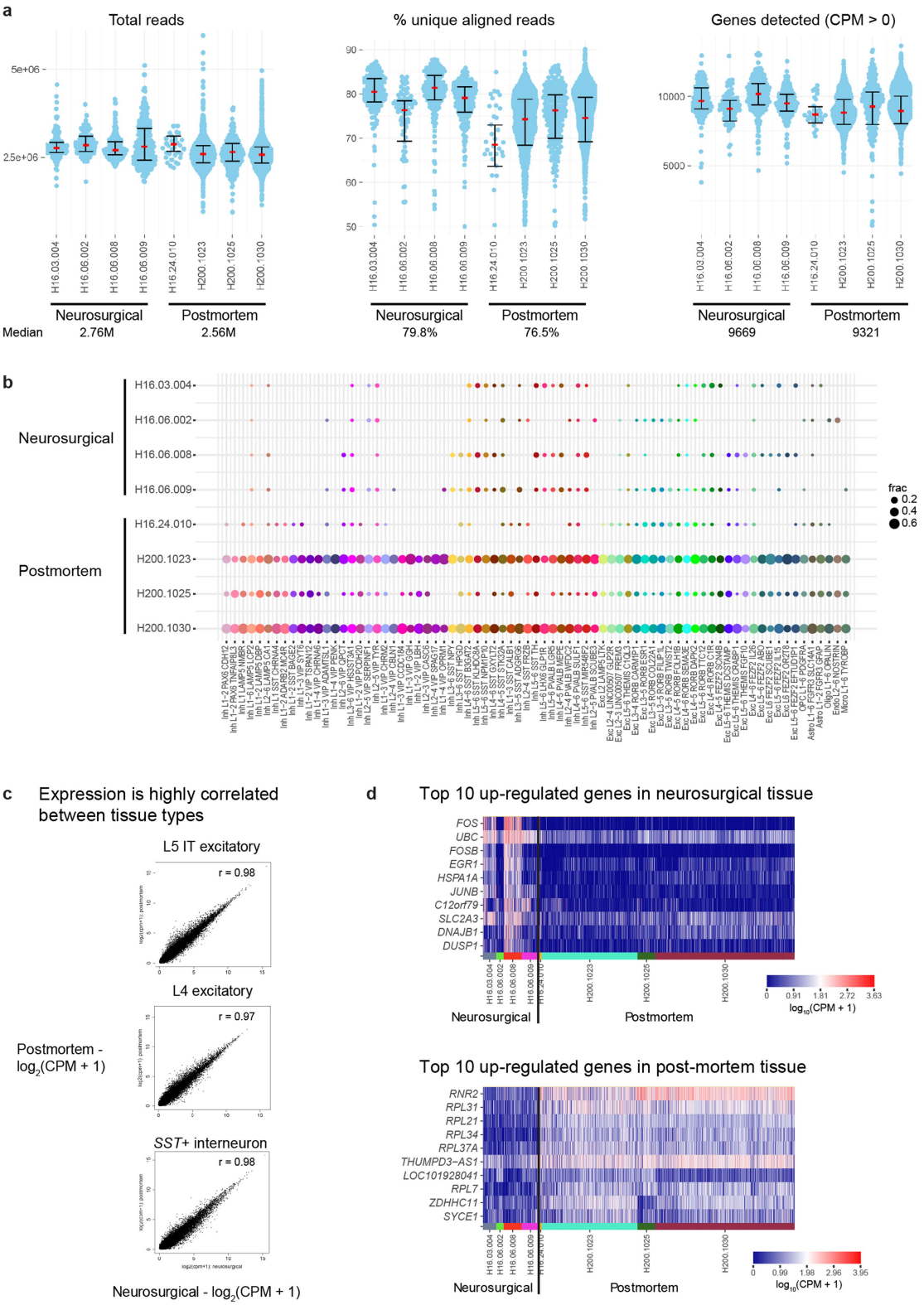

Extended Data Fig. 2 | See next page for caption.

Extended Data Fig. 2 | Small but consistent expression signature of donor tissue source. a, mRNA quality was only slightly higher for nuclei isolated from neurosurgical ($n = 722$) versus postmortem ($n = 15{,}206$) donors (~3% more uniquely aligned reads and ~350 more genes detected). All nuclei were dissected from cortical L5 and sorted on the basis of NeuN-positive staining, and transcripts were sequenced to a median depth of approximately 2.5 million reads per nucleus. Median values (red points) and interquartile interval are indicated. **b**, Dot plot showing the proportion of nuclei isolated from neurosurgical and postmortem donors among human MTG clusters. Note that most nuclei from neurosurgical donors were isolated only from L5, so clusters enriched in other layers, such as L1 interneurons, have low representation of these donors. **c**, Highly correlated (Pearson's) expression between nuclei from postmortem and neurosurgical donors among two subclasses of excitatory neurons and one subclass of inhibitory neurons. Nuclei were pooled and compared within these subclasses owing to the low sampling of individual clusters from neurosurgical donors. Average expression of $n = 2{,}180$, 1,636 and 815 postmortem nuclei and 127, 38 and 114 neurosurgical nuclei were included for the L5a excitatory, L4 excitatory and SST^{+} interneuron comparisons, respectively. **d**, Expression ($\log_{10}(\mathrm{CPM} + 1)$) heat maps of the top-10 upregulated genes in nuclei from postmortem and neurosurgical donors including ribosomal genes and activity-dependent genes, respectively.

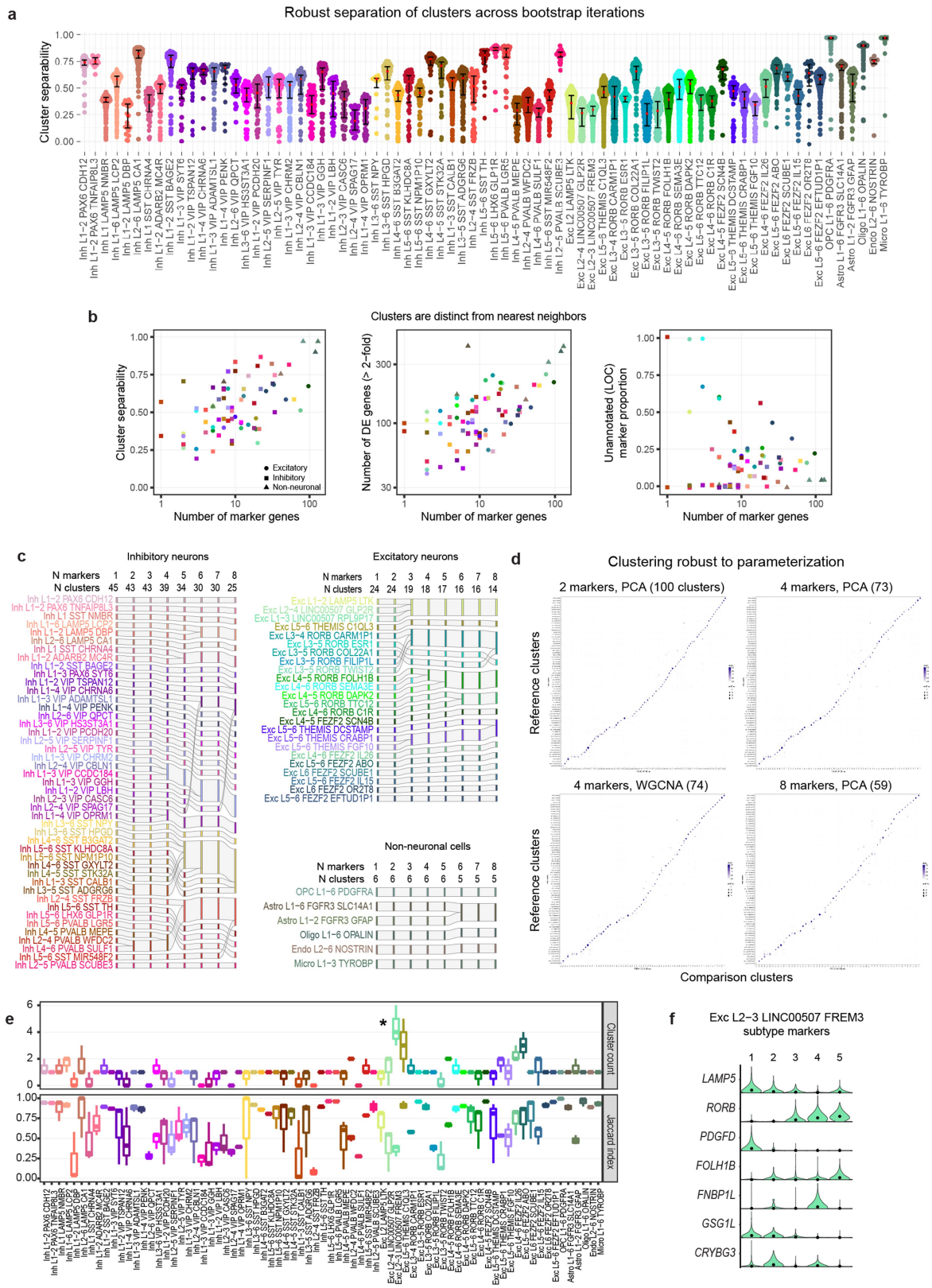

Extended Data Fig. 3 | See next page for caption.

Extended Data Fig. 3 | Cluster robustness. a, Cluster separability (mean co-clustering within a cluster minus the maximum co-clustering between clusters) varied substantially among cell types ($n = 15{,}928$ nuclei), with a subset of neuronal types and all non-neuronal types being highly discrete. **b**, Scatter plots quantifying the separation of each cluster from its nearest neighbour. Left, cluster separability based on rounds of iterative clustering using all variable genes is correlated with the number of binary marker genes. Middle, all clusters express at least 30 genes with >twofold increased expression, but only a subset are binary markers. Right, A substantial fraction of markers of many clusters are unannotated. **c**, River plots of clusters that merge with more binary markers required for separation. Note that clusters that appear distinct on the basis of layer position (excitatory neurons in L2 and L3), morphology (interlaminar astroctyes in L1) or homology with mouse (SST^{+} interneuron subtypes) can have few binary markers. Marker genes for clusters defined by four markers are listed in Supplementary Table 2. **d**, Confusion plots comparing cluster membership of single nuclei ($n = 15{,}928$) in reference MTG clusters and clusters generated using a different iterative clustering pipeline. Above each plot are listed the parameter settings and total number of clusters detected. Point size is proportional to the number of nuclei and point colour corresponds to the Jaccard index, with darker colours corresponding to a higher Jaccard index and greater consistency between clustering. **e**, Box plots summarizing consistency of cluster membership of single nuclei ($n = 15{,}928$) across the four iterative clustering runs shown in **c**. Box plots show median, interquartile interval and full range of values. Top, the number of clusters that overlap each reference cluster. A cluster count of 1 indicates a one-to-one match, 0 indicates that a reference cluster was not detected and was merged with a related cluster, and >1 indicates that a reference cluster was split into sub-clusters. *The Exc L2−3 *LINC00507 FREM3* reference cluster was consistently divided into subclusters. Bottom, reference clusters with higher Jaccard index values have more consistent membership of nuclei and therefore more distinct borders with related clusters. **f**, Violin plots of marker-gene expression for *FREM3* subclusters ($n = 2{,}284$ nuclei) identified in one clustering run show relatively binary expression. In the violin plot, rows are genes and black dots correspond to median expression. Expression values are on a linear scale.

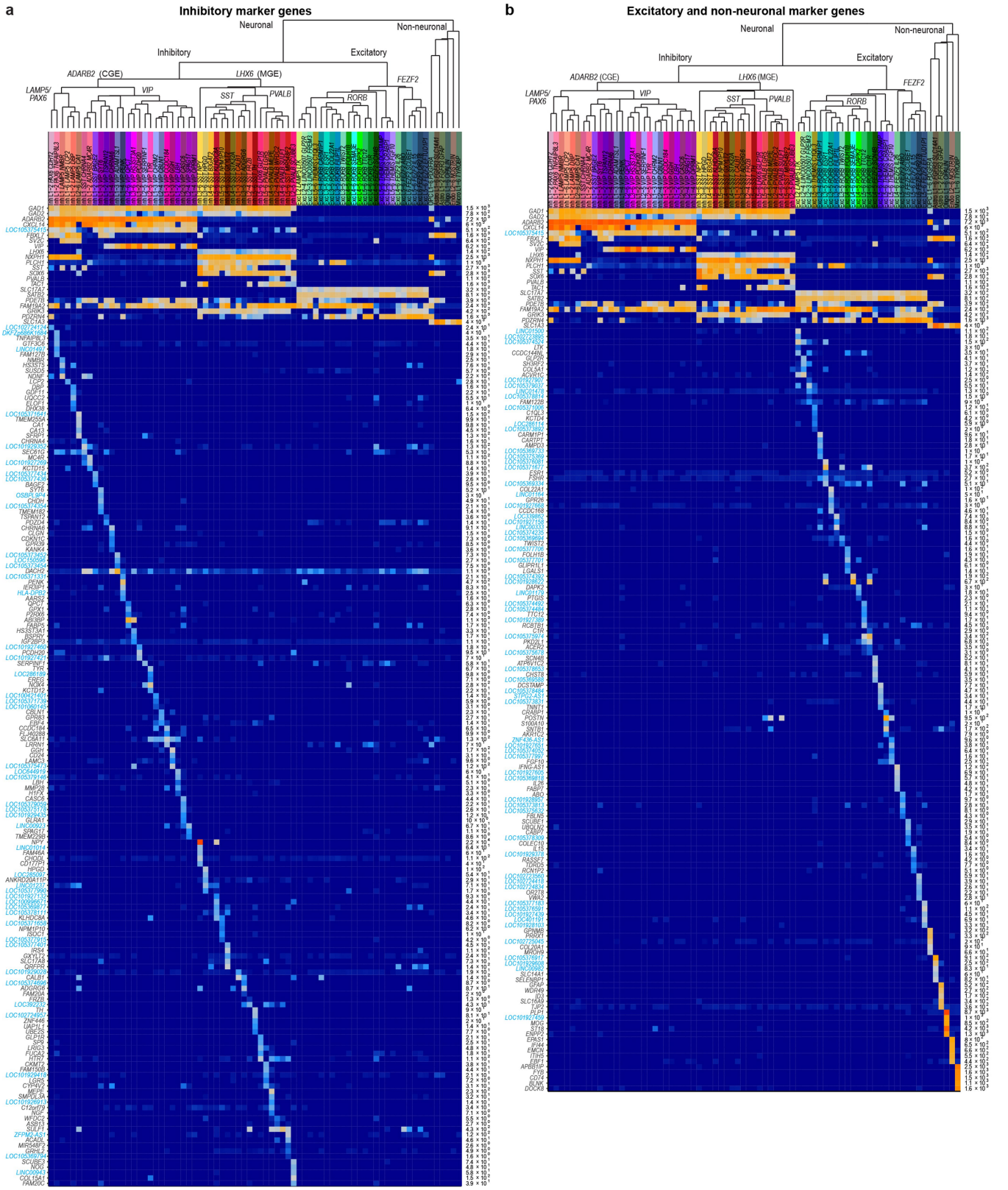

Extended Data Fig. 4 | Expression of cell-type-specific markers. **a**, **b**, Heat maps of the top cell-type markers for inhibitory neurons (**a**) and excitatory neurons and non-neuronal cell types (**b**). Markers include many non-coding and unannotated genes (blue). Median expression values are shown on a logarithmic scale, with maximum expression values shown on the right side of each row. Up to five marker genes are shown for each cell type. Note that LOC genes were excluded from cluster names, and the best non-LOC marker genes were used instead. Dendrograms and cluster names are reproduced from Fig. 1. Marker genes for broad classes, as defined manually and using NS-Forest, are also shown in the top rows of each heat map.

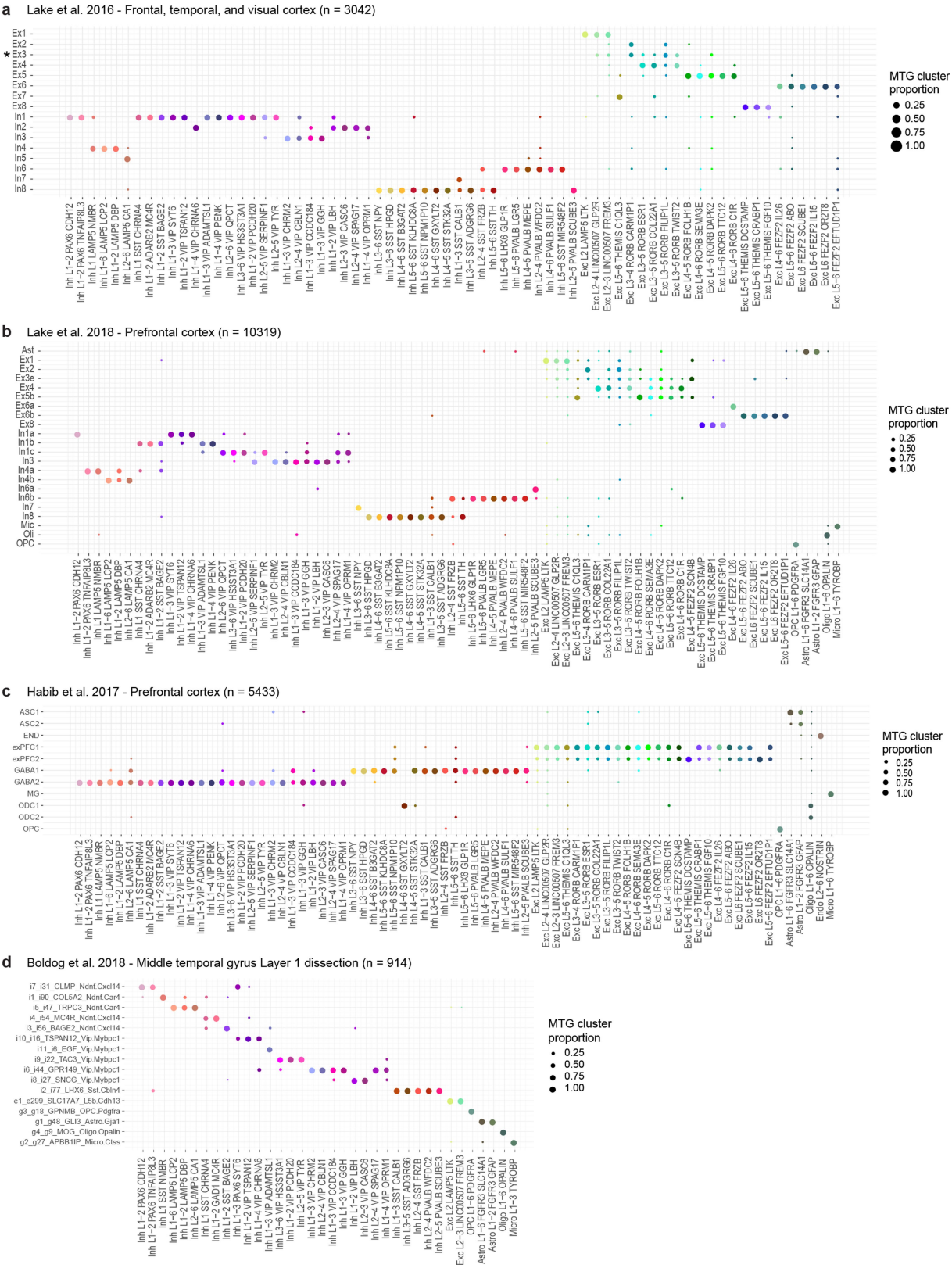

Extended Data Fig. 5 | Clusters in this study capture reported human cortical cell types and additional subtype diversity. a–c, Dot plots showing the proportion of each MTG cluster that matches reported clusters based on a centroid expression classifier. **a**, Three of sixteen neuronal clusters reported by Lake et al.[24] ($n = 3{,}042$ nuclei) match human MTG clusters one-to-one, and the remaining clusters map to multiple MTG clusters. *Ex3 was highly enriched in visual cortex and not detected in temporal cortex by Lake et al. **b**, Four of eighteen neuronal clusters and three of four non-neuronal clusters reported by Lake et al.[27] ($n = 10{,}319$ nuclei) match human MTG clusters one-to-one, including two rare but distinct interneuron types (Inh L3–6 *SST NPY* and Inh L2–5 *PVALB SCUBE3*) and one rare but distinct excitatory type (Exc L4–5 *FEZF2 SCN4B*). **c**, Four neuronal clusters reported by Habib et al.[28] ($n = 5{,}433$ nuclei) correspond to broad classes of inhibitory and excitatory neurons. Seven non-neuronal clusters include two astrocyte types that correspond to the types reported in this study, and one additional oligodendrocyte subtype. **d**, Sixteen clusters detected in L1 of human temporal cortex[14] ($n = 914$ nuclei) are captured at finer subtype resolution in this study.

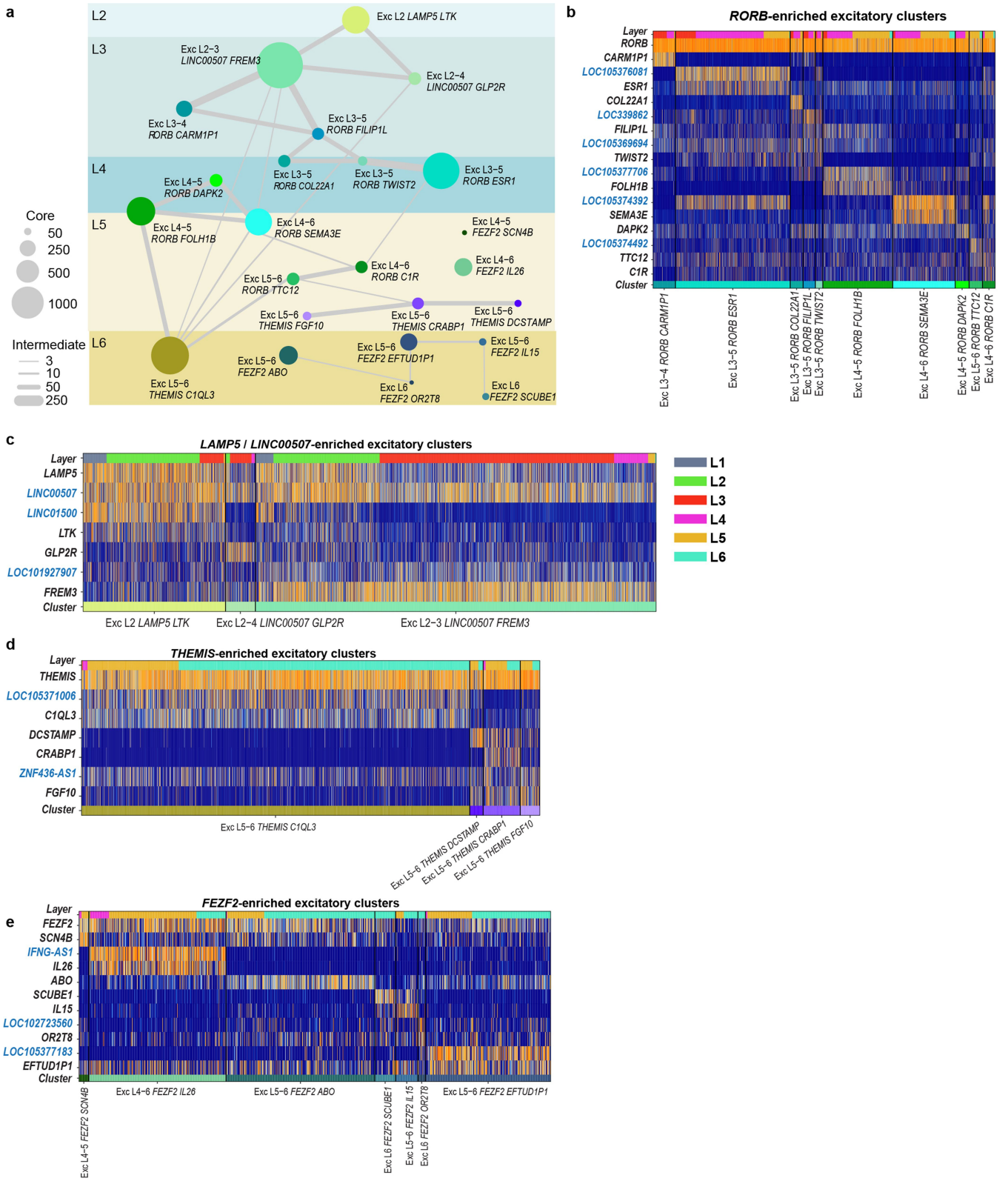

Extended Data Fig. 6 | Excitatory neuron types express marker genes across multiple cortical layers. a, Constellation diagram showing cluster relationships, relative frequencies and average layer position. **b–e**, Heat maps of log-transformed expression in individual nuclei ordered by cluster and then layer. Clusters are grouped on the basis of their dominant class-marker gene, which corresponds to position in superficial (*LAMP5/LINC00507*, **c**; *RORB*, **b**) and deep (*THEMIS*, **d**; *FEZF2*, **e**) layers.

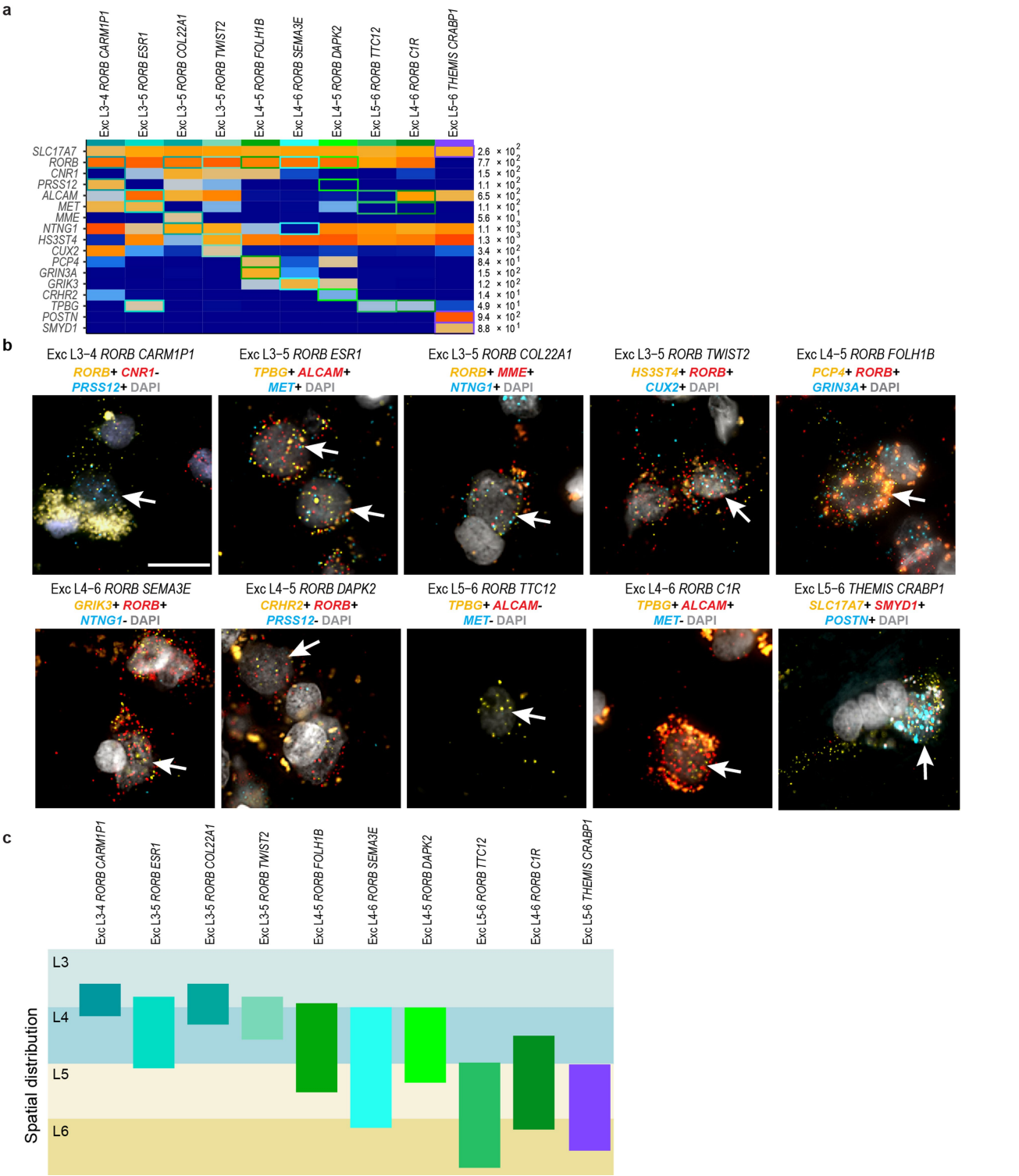

Extended Data Fig. 7 | RNAscope mFISH validation of ten excitatory neuron types. a, Heat map summarizing combinatorial three-gene panels used for multiplex FISH assays to explore the spatial distribution of ten excitatory clusters. Gene combinations for each cluster are indicated by coloured boxes on the heat map. Maximum expression values for each gene are listed on the right of the heat map and gene-expression values are displayed on a log scale. Experiments were repeated on at least two donors for each probe combination with similar results. **b**, Gene combinations probed are listed above each image. Labelled cells are indicated by white arrows. Scale bar, 20 μm. **c**, Schematic representing the laminar distribution of clusters on the basis of the observed positions of labelled cells across at least three sections from at least two donors per cell type.

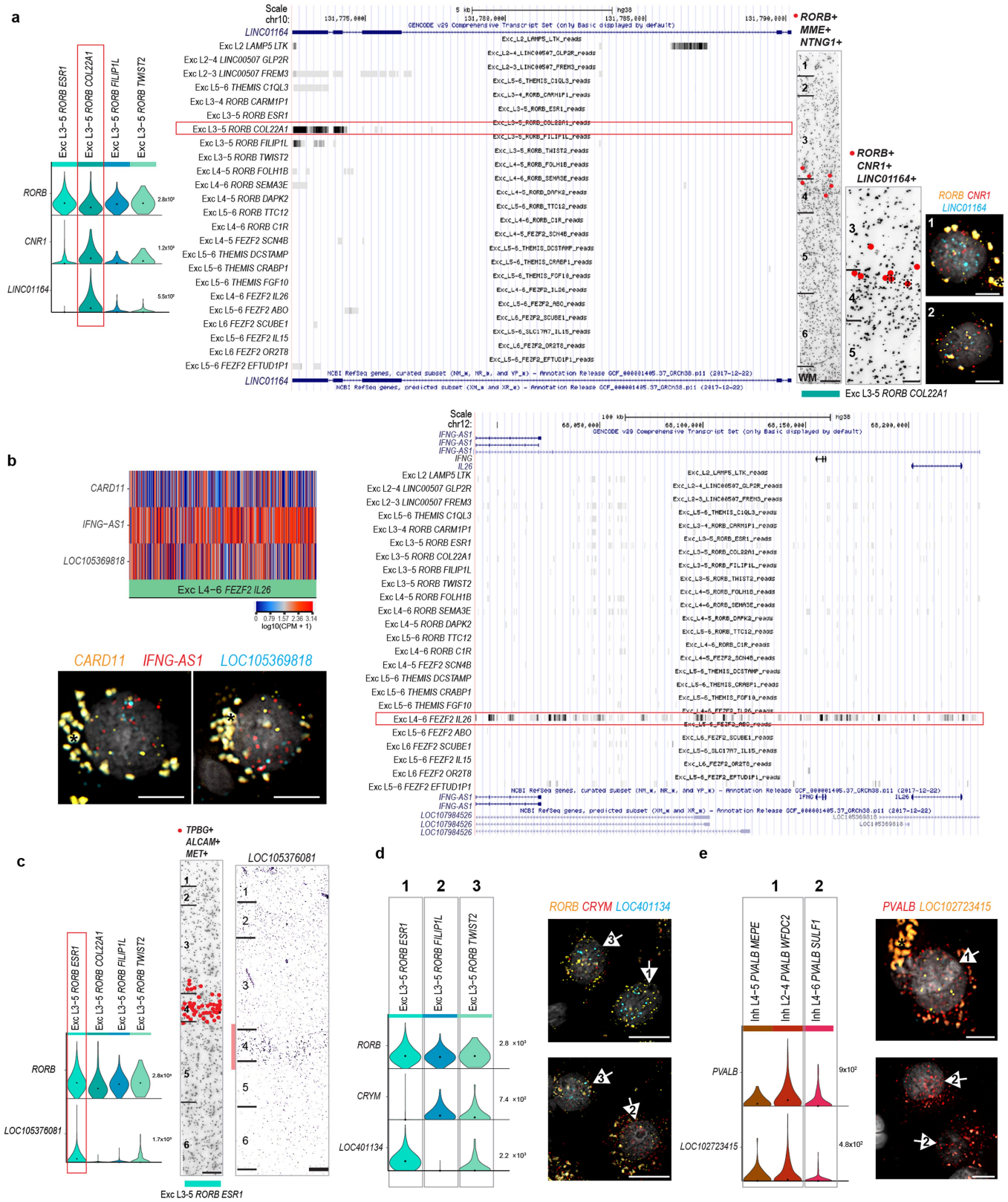

Extended Data Fig. 8 | See next page for caption.

Extended Data Fig. 8 | In situ validation of LOC, long non-coding RNA and antisense transcripts as cell-type-specific markers. a, *LINC01164* specifically labels the Exc L3–5 *RORB COL22A1* cluster ($n = 160$ nuclei). Left, violin plots showing expression of genes used for cluster validation by mFISH. Middle, read pile-ups shown for *LINC01164* across all excitatory clusters ($n = 24$), viewed in UCSC genome browser. Red box indicates Exc L3–5 *RORB COL22A1* cluster. Right, mFISH validation of cluster-specific marker genes. Laminar distribution of the Exc L3–5 *RORB COL22A1* cluster marked by *LINC01164* is consistent with the distribution shown using protein-coding marker genes (panel showing staining for *RORB*, *MME* and *NTNG1* reproduced from Fig. 2c). Scale bars, 100 μm (low-magnification DAPI-stained columns); 5 μm (mFISH images). Experiments were repeated on two donors with similar results. **b**, The Exc L4–6 *FEZF2 IL26* cluster ($n = 344$ nuclei) is specifically marked by *INFG-AS1* and *LOC105369818*. Top, heat map showing expression of these genes along with protein-coding marker gene *CARD11*. Bottom, mFISH validation of cluster-specific marker genes. Experiments were repeated on three donors with similar results. Scale bars, 5 μm. Right, read pile-ups shown for *INFG-AS1* across all excitatory clusters, viewed in UCSC genome browser. Red box indicates Exc L4–6 *FEZF2 IL26* cluster. **c**, Violin plots showing expression of *LOC105376081* in the Exc L3–5 *RORB ESR1* cluster ($n = 1{,}428$ nuclei). Right, ISH for *LOC105376081* shows expression in L4 (red bar), consistent with the anatomical location of Exc L3–5 *RORB ESR1* (left, laminar distribution from Fig. 2). Scale bars, 100 μm. **d**, Violin plots showing expression of *LOC401134* and the protein-coding gene *CRYM* in three L3–5 *RORB*-expressing clusters ($n = 1{,}674$ nuclei). Right, mFISH showing three possible combinations for the genes assayed as indicated by labelled arrows. Scale bars, 10 μm. Experiments were repeated on two donors with similar results. **e**, *LOC102723415* labels a subset of *PVALB* clusters ($n = 618$ nuclei) as shown in the violin plots on the left and mFISH images on the right (clusters indicated by labelled arrows). Scale bars, 5 μm. Experiments were repeated on two donors with similar results. For all violin plots, rows are genes, black dots correspond to median expression and maximum expression (CPM) is listed on the far right. Expression values are on a linear scale. Asterisks indicate lipofuscin in mFISH images.

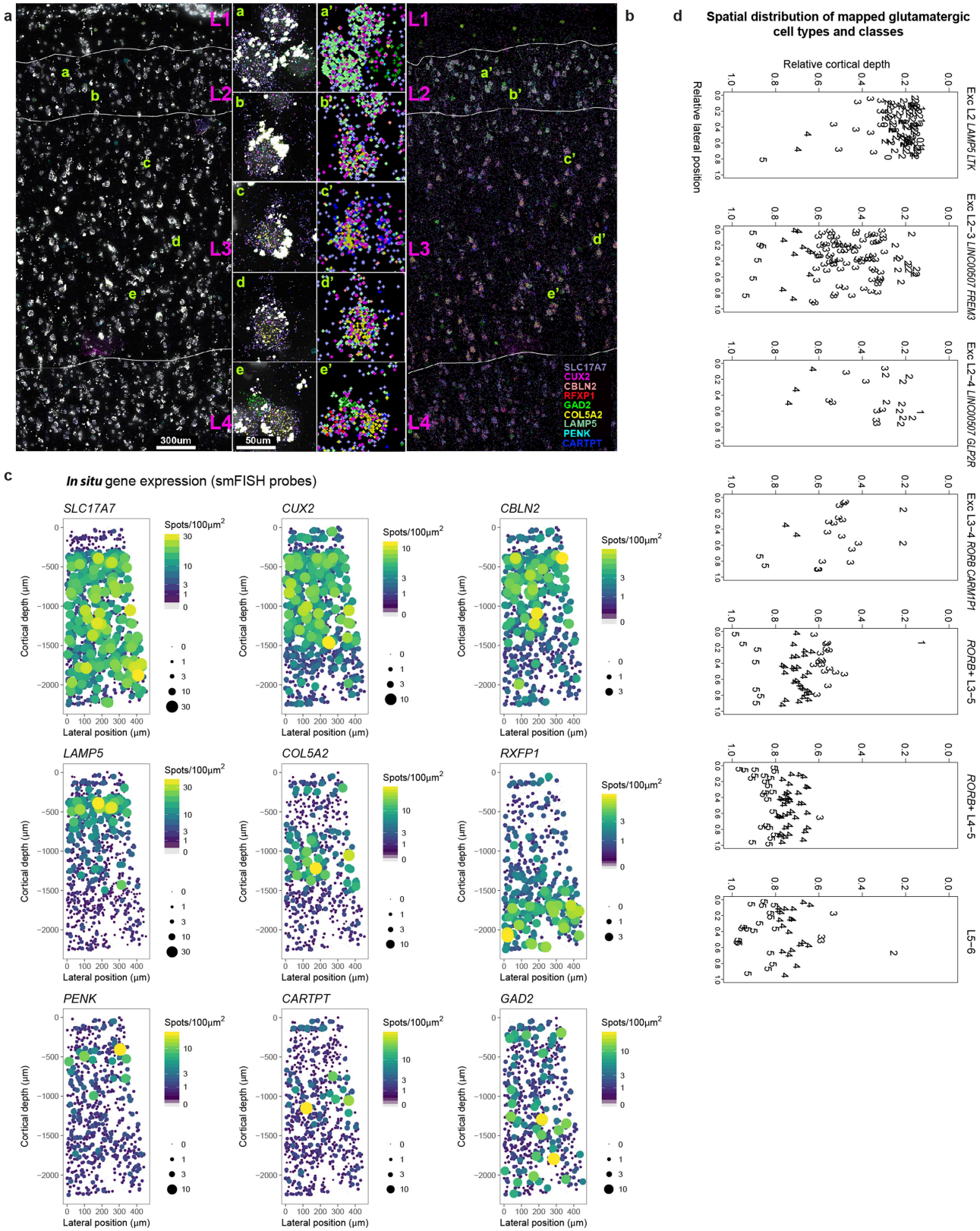

Extended Data Fig. 9 | See next page for caption.

Extended Data Fig. 9 | Laminar distribution of superficial excitatory neuron types validated by smFISH. a, smFISH (image, 100×) was performed with probes against *SLC17A7*, *CUX2*, *CBLN2*, *RFXP1*, *GAD2*, *COL5A2*, *LAMP5*, *PENK* and *CARTPT* mRNA. Spots for each gene are pseudocoloured as indicated in the bottom right legend. Layer demarcations are indicated in magenta. Scale bar, 300 μm. **b**, Spot indications for each gene, pseudocoloured as indicated in the bottom right legend, as in **a**. a,a′, Superficial L2 cells express *SLC17A7*(lavender), *CUX2* (magenta) and *LAMP5* (mint). b,b′, At deeper locations in L2, an example of an *SLC17A7*-expressing cell with *CUX2*, *LAMP5* and *COL5A2* expression. Note that *LAMP5* expression (mint) decreases in *CUX2*/*SLC17A7*-expressing cells, whereas *COL5A2*/*CUX2*-expressing cells increase with depth along L2 and L3 (see, c,c′; d,d′; e,e′). **c**, Probe density (spots per 100 μm^2) for nine genes assayed across L1–L4 (and partially L5) of human MTG. The cortical slice was approximately 0.5 mm wide and 2 mm deep. Points correspond to cellular locations in situ where the *y* axis is the cortical depth from the pial surface and the *x* axis is the lateral position. Point size and colour correspond to probe density. Cells that lack probe expression are shown as small grey points. Experiments were repeated on three donors with similar results. **d**, In situ location of cells mapped to indicated cell types and classes (different panels) on the basis of expression levels of nine genes shown in **a**. Numbers indicate qualitative calls of the layer to which each cell belongs based on cytoarchitecture, and 0 indicates that the cell was not annotated.

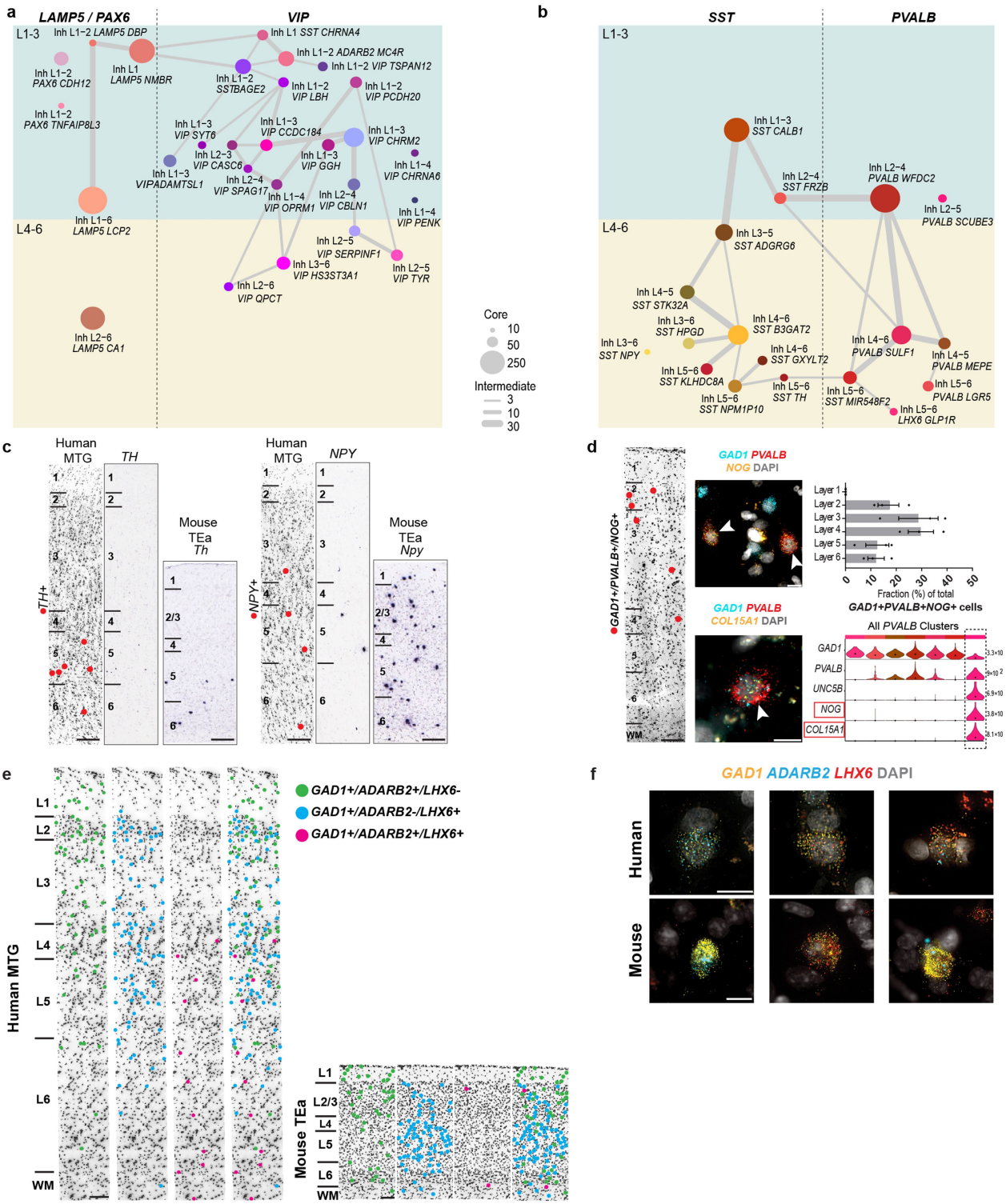

Extended Data Fig. 10 | See next page for caption.

Extended Data Fig. 10 | Layer distributions and frequencies of inhibitory neuron types. a, **b**, Constellation diagram showing cluster relationships, relative frequencies and average layer position for *LAMP5/PAX6* ($n = 2{,}320$ nuclei) (**a**) and *SST/PVALB* ($n = 1{,}844$ nuclei) (**b**) classes of inhibitory neurons. **c**, Chromogenic ISH for *TH*, a marker of Inh L5–6 *SST TH* and *NPY*, a marker of Inh L3−6 *SST NPY*, from the Allen Human Brain Atlas. Left columns show greyscale images of the Nissl section nearest the ISH section shown on the right for each gene. Red dots show cells positive for the gene assayed by ISH. Experiments were repeated 9 (*NPY*) and 40 (*TH*) times with similar results. Chromogenic ISH for *Th* and *Npy* in mouse TEa from the Allen Mouse Brain Atlas are to the right of the human images. Experiments were repeated six (*Npy*) and two (*Th*) times with similar results. Scale bars, human, 250 μm; mouse, 100 μm. **d**, RNAscope mFISH for markers of Inh L2−5 *PVALB SCUBE3*. Left, inverted DAPI-stained cortical column with red dots marking cells positive for the genes *GAD1*, *PVALB* and *NOG* (scale bar, 250 μm). Middle, cells positive for *GAD1*, *PVALB* and the specific marker genes *NOG* (top: scale bar, 10 μm) and *COL15A1* (bottom: scale bar, 10 μm). White arrows mark triple-positive cells. Experiments were repeated on three donors with similar results. Right, counts of $GAD1^{+}PVALB^{+}NOG^{+}$ cells across layers (expressed as percentage of total triple-positive cells). Data are mean ± s.d. and dots show the data points for individual specimens ($n = 3$ subjects). Violin plots show gene-expression distributions across clusters in the *PVALB* subclass ($n = 802$ nuclei) for the chandelier cell marker *UNC5B* and the Inh L2−5 *PVALB SCUBE3* cluster markers *NOG* and *COL15A1*. Rows are genes, black dots correspond to median expression and maximum expression (CPM) is listed on the far right. Expression values are on a linear scale. **e**, Inverted DAPI-stained cortical column illustrating laminar positions of cells labelled with interneuron class markers. Green dots mark $GAD1^{+}/Gad1^{+}$, $ADARB2^{+}/Adarb2^{+}$ and $LHX6^{-}/Lhx6^{-}$ cells (that is, *ADARB2* branch interneurons); blue dots mark $GAD1^{+}/Gad1^{+}$, $ADARB2^{-}/Adarb2^{-}$ and $LHX6^{+}/Lhx6^{+}$ cells (that is, *LHX6* branch interneurons); and pink dots mark $GAD1^{+}/Gad1^{+}$, $ADARB2^{+}/Adarb2^{+}$ and $LHX6^{+}/Lhx6^{+}$ cells (that is, Inh L2–6 *LAMP5 CA1* cells in human or *Lamp5 Lhx6* cells in mouse). **f**, Representative images of cells labelled with the *GAD1, ADARB2* and *LHX6* gene panel for human (top) and mouse (bottom). Left to right: cells double positive for *GAD1* and *ADARB2*; cells double positive for *GAD1* and *LHX6*; and *GAD1*, *ADARB2* and *LHX6* triple-positive cells. Scale bars, 15 μm (human), 10 μm (mouse). Experiments were repeated on three donors and three mice with similar results.

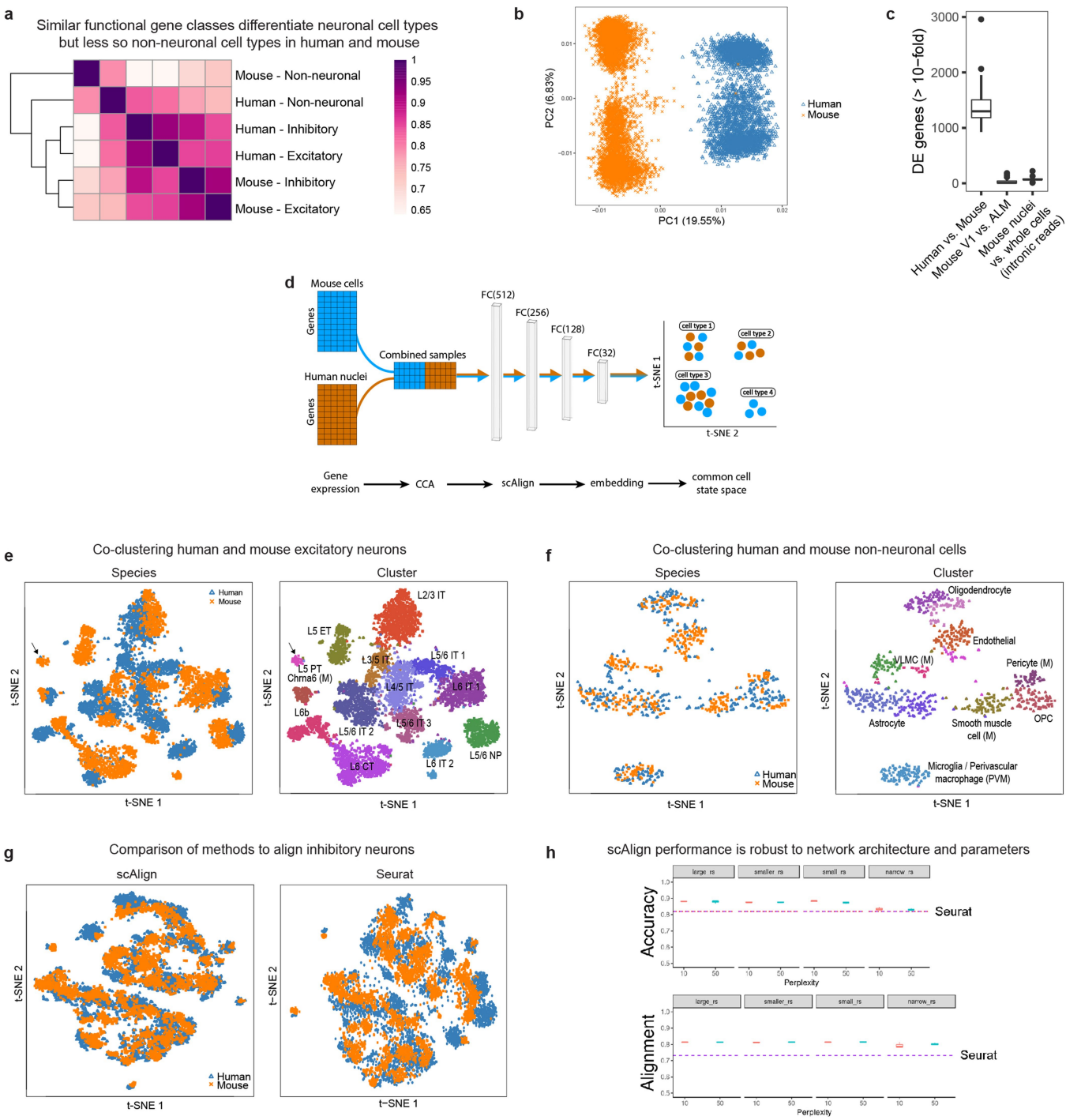

Extended Data Fig. 11 | Aligning snRNA-seq and scRNA-seq data from human and mouse cortex. a, Heat map of Pearson's correlations between average MetaNeighbour AUROC scores ($n = 384$ gene sets) for three broad classes of human and mouse cortical cell types. Rows and columns are ordered by average-linkage hierarchical clustering. **b**, Human (blue; $n = 3{,}594$ nuclei) and mouse (orange; $n = 6{,}595$ cells) inhibitory neurons projected on the first two principal components of a PCA combining expression data from both species. Almost 20% of expression differences are explained by species, whereas 6% are explained by major classes of interneurons. **c**, Number of highly differentially expressed (>tenfold change) genes (out of 14,551 orthologous genes) between homologous cell types matched between species ($n = 37$ types), mouse cortical area[22] ($n = 103$ types) and sample type[26] ($n = 11$ types). Box plots show median, interquartile interval, range and outlier values. **d**, Schematic of scAlign analysis to align RNA-seq data from human nuclei and mouse cells. **e**, *t*-SNE plots of human (blue; $n = 3{,}503$ nuclei) and mouse (orange; $n = 4{,}127$ cells) excitatory neurons after alignment with scAlign and coloured by species and cluster. Arrow highlights two human nuclei that cluster with the mouse-specific (M) L5 PT *Chrna6* cluster. **f**, *t*-SNE plots of human (blue; $n = 670$ nuclei) and mouse (orange; $n = 671$ cells) non-neuronal cells coloured by species and cluster. **g**, *t*-SNE plots of human (blue; $n = 3{,}594$ nuclei) and mouse (orange; $n = 6{,}595$ cells) inhibitory neurons after alignment with scAlign (as in Fig. 5c) and Seurat and coloured by species. **h**, Consistently higher accuracy and alignment of inhibitory neurons using scAlign versus Seurat with several neural network architectures and parameter settings. Box plots show median and interquartile interval of values.

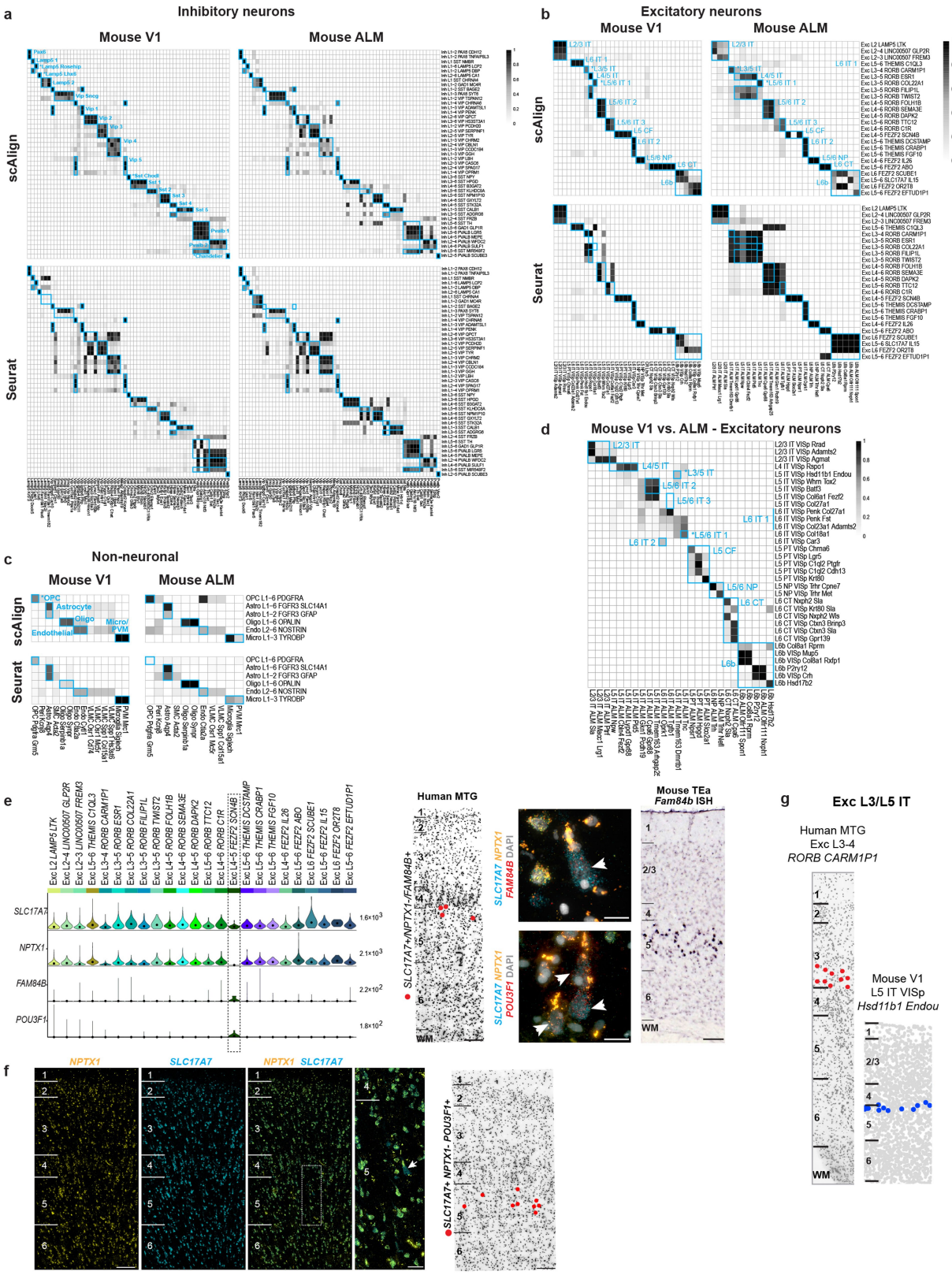

Extended Data Fig. 12 | See next page for caption.

Extended Data Fig. 12 | Quantifying human and mouse cell-type homology and comparing cell-type frequencies between species. **a–c**, Heat maps with inferred cell-type homologies highlighted in blue boxes. For each pair of clusters, the shade of grey indicates the minimum proportion of samples that co-cluster. Homologies for human and mouse inhibitory neurons (**a**), excitatory neurons (**b**) and non-neuronal cells (**c**) were predicted on the basis of shared cluster membership using mouse cells from two cortical areas (V1 and ALM) and two unsupervised alignment algorithms (scAlign and Seurat). **d**, Mouse V1 and mouse ALM excitatory neurons were aligned with scAlign. Blue boxes indicate V1 and ALM clusters that align to the same human clusters in **b** and are members of homologous cell types. Note that cell types can be matched at higher resolution within species than between species, as expected. **e**, Left to right: violin plots ($n = 10{,}525$ nuclei) showing expression of specific markers of the putative extratelencephalic EXC L4–5 *FEZF2 SCN4B* cluster (black box) and *NPTX1*, a gene expressed by all non-PT excitatory neurons. Each row represents a gene, the black dots in each violin represent median gene expression within clusters, and the maximum expression value for each gene is shown on the right-hand side of each row. Expression values are shown on a linear scale. Representative inverted DAPI-stained cortical column (scale bar, 200 μm) with red dots marking the position of cells positive for the genes *SLC17A7* and *FAM84B* and negative for *NPTX1* illustrates the relative abundance of the EXC L4–5 *FEZF2 SCN4B* type in human MTG. Representative examples (arrows) of *FAM84B* (scale bar, 25 μm) and *POU3F1*-expressing cells (scale bar, 25 μm). Expression of *Fam84b* in mouse TEa (scale bar, 75 μm) is shown in the adjacent panel. **f**, mFISH for *NPTX1*, a marker of non-PT excitatory types and *SLC17A7*, shows that *NPTX1* labels most *SLC17A7*$^+$ cells across all cortical layers. Boxed region shown at higher the magnification to the right. One *SLC17A7*$^+$ cell (white arrow) is *NPTX1*$^-$, but all other all other *SLC17A7*$^+$ cells are *NPTX1*$^+$. Scale bars, 200 μm (left); 50 μm (right). Right, representative inverted DAPI-stained cortical column with red dots that represent *SLC17A7*$^+$, *NPTX1*$^-$ and *POU3F1*$^+$ cells. Scale bar, 200 μm. **e**, **f**, Experiments were repeated on three donors (human) and two mice with similar results. **g**, ISH validation of layer distributions in human MTG and mouse primary visual cortex (data from ref. [22]). Cells are labelled by cluster marker genes in human (*RORB*$^+$/*CNR1*$^-$/*PRSS12*$^+$) and mouse (*Scnn1a*$^+$/*Hsd11b1*$^+$). ISH was performed on three human donors with similar results. For mouse, one experiment was performed.

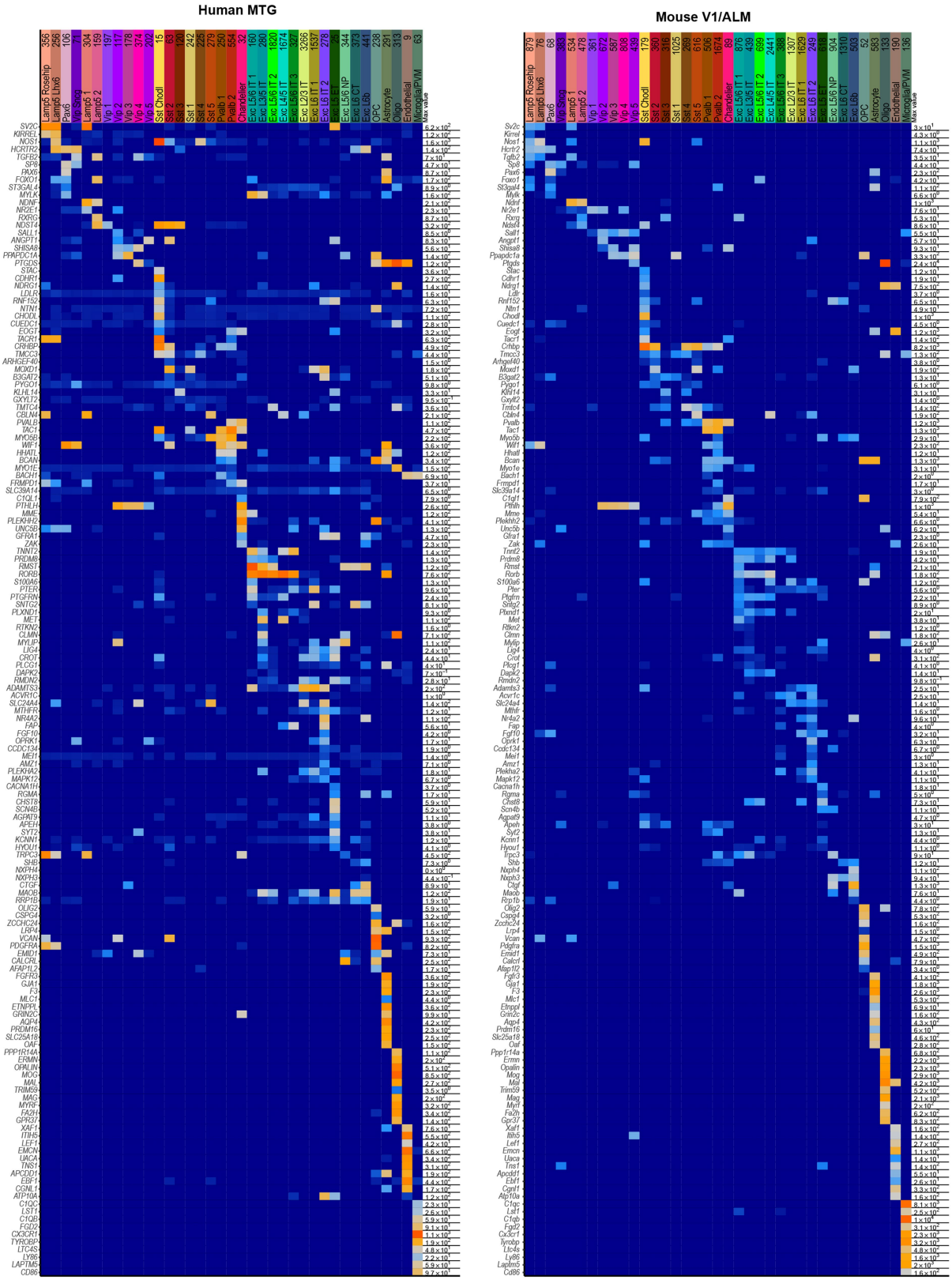

Extended Data Fig. 13 | Marker genes with relatively conserved expression in homologous cell types between human and mouse. Expression heat maps of homologous cell-type markers in human cortical nuclei and mouse cortical cells. Rows, median expression based on intronic and exonic reads and log-transformed ($\log_{10}(\mathrm{CPM}+1)$). Values listed on the right side of each heat map indicate the maximum expression level (CPM) for each gene. Columns: single nuclei (human) or cells (mouse) grouped by homologous types identified in this study. For each homologous type, up to ten marker genes were identified based on relatively specific expression (median CPM >1 in six or fewer clusters and ordered by τ score) in both species. Note that many more genes support individual homologies but may not be cell-type-specific markers.

Extended Data Table 1 | Summary of human tissue donor information

Specimen ID	Tissue Type	Age	Sex	Race	Cause of Death	PMI (hr)	Tissue RIN	Hemisphere Sampled	Reason for Surgery	Number of nuclei sampled
H200.1023	P	43	F	Iranian descent	Mitral valve prolapse	18.5	7.4 ± 0.7	L	N/A	6170
H200.1025	P	50	M	Caucasian	CV	24.5	7.6 ± 1.0	L	N/A	1334
H200.1030	P	54	M	Caucasian	CV	25	7.7 ± 0.8	L	N/A	7331
H16.24.010	P	66	M	Caucasian	CV	21	7.2 ± 1.4	L	N/A	371
H16.06.002	N	35	F	Caucasian	N/A	N/A	7.1 ± 0.9	R	Epilepsy	97
H16.06.008	N	24	F	Hispanic	N/A	N/A	8.1 ± 0.8	L	Epilepsy	197
H16.06.009	N	48	F	Caucasian	N/A	N/A	7.1	L	Epilepsy	220
H16.03.004	N	25	M	Not noted	N/A	N/A	8.2 ± 0.8	R	Tumor removal, epilepsy	208

Tissue types: P, postmortem; N, neurosurgical. Cause of death: CV, cardiovascular; N/A, not applicable. PMI, postmortem interval; RIN, RNA integrity number. Tissue RIN was measured using three tissue samples per donor, except for H16.06.009, for which RIN was derived from a single tissue sample. Values listed are the mean ± s.d.

nature research

Corresponding author(s): Ed Lein

Reporting Summary

Nature Research wishes to improve the reproducibility of the work that we publish. This form provides structure for consistency and transparency in reporting. For further information on Nature Research policies, see Authors & Referees and the Editorial Policy Checklist.

Statistical parameters

When statistical analyses are reported, confirm that the following items are present in the relevant location (e.g. figure legend, table legend, main text, or Methods section).

n/a	Confirmed	
☐	☒	The exact sample size (*n*) for each experimental group/condition, given as a discrete number and unit of measurement
☐	☒	An indication of whether measurements were taken from distinct samples or whether the same sample was measured repeatedly
☐	☒	The statistical test(s) used AND whether they are one- or two-sided *Only common tests should be described solely by name; describe more complex techniques in the Methods section.*
☒	☐	A description of all covariates tested
☐	☒	A description of any assumptions or corrections, such as tests of normality and adjustment for multiple comparisons
☐	☒	A full description of the statistics including central tendency (e.g. means) or other basic estimates (e.g. regression coefficient) AND variation (e.g. standard deviation) or associated estimates of uncertainty (e.g. confidence intervals)
☐	☒	For null hypothesis testing, the test statistic (e.g. *F*, *t*, *r*) with confidence intervals, effect sizes, degrees of freedom and *P* value noted *Give P values as exact values whenever suitable.*
☒	☐	For Bayesian analysis, information on the choice of priors and Markov chain Monte Carlo settings
☒	☐	For hierarchical and complex designs, identification of the appropriate level for tests and full reporting of outcomes
☒	☐	Estimates of effect sizes (e.g. Cohen's *d*, Pearson's *r*), indicating how they were calculated
☐	☒	Clearly defined error bars *State explicitly what error bars represent (e.g. SD, SE, CI)*

Our web collection on statistics for biologists may be useful.

Software and code

Policy information about availability of computer code

Data collection	BD Diva software v8.0, Nikon NIS-Elements Advanced Research imaging software v4.20, SoftMax Pro v6.5; VWorks v11.3.0.1195 and v13.1.0.1366; Hamilton Run Time Control v4.4.0.7740; Fragment Analyzer v1.2.0.11; Mantis Control Software v3.9.7.19; Illumina HiSeq 2500 instrument control software.
Data analysis	FIJI distribution of ImageJ, GraphPad Prism v7.04. Paired-end reads were mapped using Spliced Transcripts Alignment to a Reference (STAR) using default settings. R packages GenomicAlignments, limma, MetaNeighbor (https://github.com/maggiecrow/MetaNeighbor), ggplot. Seurat package is available at https://satijalab.org/seurat/. ScAlign is available at https://github.com/quon-titative-biology/scAlign. Custom R code written for clustering single nucleus RNA-seq data and marker gene analysis and using open source R packages is available from https://github.com/AllenInstitute/MTG_celltypes. The NSforest code is available at https://github.com/JCVenterInstitute/NSForest.

For manuscripts utilizing custom algorithms or software that are central to the research but not yet described in published literature, software must be made available to editors/reviewers upon request. We strongly encourage code deposition in a community repository (e.g. GitHub). See the Nature Research guidelines for submitting code & software for further information.

Data

Policy information about availability of data

All manuscripts must include a data availability statement. This statement should provide the following information, where applicable:

- Accession codes, unique identifiers, or web links for publicly available datasets
- A list of figures that have associated raw data
- A description of any restrictions on data availability

Data and code used to produce figures are available from https://github.com/AllenInstitute/MTG_celltypes. Data can be accessed through the Allen Brain Atlas data portal at http://portal.brain-map.org/ and RNA-seq data from this study is publicly available and can be downloaded at http://celltypes.brain-map.org/. Data can be visualized and analyzed using two complementary viewers, the RNA-seq Data Navigator (http://celltypes.brain-map.org/rnaseq/human) and the Cytosplore Viewer (https://viewer.cytosplore.org/), an extension of Cytosplore (T. Höllt 2016) that presents a hierarchy of t-SNE maps of different subsets of MTG clusters (Hollt 2018). An ontology of cell types can be navigated at http://bioportal.bioontology.org/ontologies/PCL. RNA-seq data has been registered with dbGAP and deposited at NeMO (https://nemoarchive.org/) and a link to controlled access raw sequencing data will be available at: http://portal.brain-map.org/explore/transcriptome as well as dbGAP (https://www.ncbi.nlm.nih.gov/projects/gap/cgi-bin/study.cgi?study_id=phs001790.v1.p1). The dbGAP accession number for this submission is: phs001790.

Field-specific reporting

Please select the best fit for your research. If you are not sure, read the appropriate sections before making your selection.

☒ Life sciences ☐ Behavioural & social sciences ☐ Ecological, evolutionary & environmental sciences

For a reference copy of the document with all sections, see nature.com/authors/policies/ReportingSummary-flat.pdf

Life sciences study design

All studies must disclose on these points even when the disclosure is negative.

Sample size

Sample size was not pre-determined. Single nuclei were isolated from postmortem brains of 4 donors and neurosurgically derived tissues from 4 donors. This allowed us to collect nuclei from high quality specimens that met stringent quality control metrics while also confirming that transcriptomic clusters were consistent between donors and not driven by technical artifacts.

Data exclusions

Poor quality nuclei were excluded from clustering if they failed to meet the following pre-established quality control (QC) thresholds:

>30% cDNA longer than 400 base pairs
>500,000 reads aligned to exonic or intronic sequence
>40% of total reads aligned
>50% unique reads
TA nucleotide ratio > 0.7

After clustering, a small number (n=325) of nuclei were excluded from further analysis if they fell into outlier or donor-specific clusters.
Outlier Clusters:
Clusters were identified as outliers if more than half of nuclei co-expressed markers of inhibitory (GAD1, GAD2) and excitatory (SLC17A7) neurons or were NeuN+ but did not express the pan-neuronal marker SNAP25. Median values of QC metrics listed above were calculated for each cluster and used to compute the median and inter-quartile range (IQR) of all cluster medians. Clusters were also identified as outliers if the cluster median QC metrics deviated by more than three times the IQRs from the median of all clusters.

Donor-specific clusters:
Clusters were identified as donor-specific if they included fewer nuclei sampled from donors than expected by chance. For each cluster, the expected proportion of nuclei from each donor was calculated based on the laminar composition of the cluster and laminar sampling of the donor. For example, if 30% of layer 3 nuclei were sampled from a donor, then a layer 3-enriched cluster should contain approximately 30% of nuclei from this donor. In contrast, if only layer 5 were sampled from a donor, than the expected sampling from this donor for a layer 1-enriched cluster was zero. If the difference between the observed and expected sampling was greater than 50% of the number of nuclei in the cluster, then the cluster was flagged as donor-specific and excluded.

To confirm exclusion, clusters automatically flagged as outliers or donor-specific were manually inspected for expression of broad cell class marker genes, mitochondrial genes related to quality, and known activity-dependent genes.

Replication

Flow cytometry data were reproducible across human tissue specimens from the 8 donor used in the study and across different nuclei isolations from individual tissue donors.

Reproducibility of clustering results was measured by performing clustering analysis 100 times using a randomly-selected 80% of cells. Next, we assessed the robustness of clusters using a similar clustering pipeline that was recently used to identify cortical cell types in mouse V1 and ALM (Tasic et al., Nature, 2018 doi: 10.1038/s41586-018-0654-5). This pipeline was run with four parameter settings, and the clustering results were compared to the reference clusters defined by the initial clustering pipeline. Confusion matrices were computed for each comparison and the Jaccard index was computed for all cluster pairs, and these results were summarized using boxplots as shown in Extended Data Figure 3.

For in situ hybridization and immunohistochemistry experiments, the number of times an experiment was repeated with similar results is listed in relevant figure legends. In general, experiments using human tissues were repeated on at least 2 independent donor tissues. For data from the Allen Brain Atlas, the number of replicates available on the website is listed in relevant figure legends for each gene shown in the paper.

Randomization

All human specimens were controls and were therefore allocated into the same experimental group. Randomization was not used. Likewise, all mouse specimens used were controls and were allocated into the same experimental group without randomization.

Blinding

Human specimens were de-identified and assigned a unique numerical code. Researchers had access to basic information about donors (age, sex, ethnicity) as well as the unique numerical code assigned to each donor.

Reporting for specific materials, systems and methods

Materials & experimental systems

n/a	Involved in the study
☒	☐ Unique biological materials
☐	☒ Antibodies
☒	☐ Eukaryotic cell lines
☒	☐ Palaeontology
☐	☒ Animals and other organisms
☐	☒ Human research participants

Methods

n/a	Involved in the study
☒	☐ ChIP-seq
☐	☒ Flow cytometry
☒	☐ MRI-based neuroimaging

Antibodies

Antibodies used

mouse anti-NeuN-PE conjugated EMD Millipore, Milli-Mark, clone A60, #FCMAB317PE
mouse anti-GFAP, Sigma-Aldrich, #G3893, clone G-A-5
mouse anti-GFAP, EMD Millipore, #MAB360, clone GA5, 1:1500
Mouse Secondary Reagent (Biocare #IPSC5001G20)
goat anti-mouse IgG(H+L) Alexa Fluor 568 conjugate, ThermoFisher Scientific, #A-11004
mouse IgG1,k PE Isotype control, clone MOPC-21,#555749, BD Pharmingen

Validation

1. mouse anti-NeuN-PE conjugated EMD Millipore, Milli-Mark, clone A60, #FCMAB317PE: evaluated by flow cytometry using U251 cells.
2. Mouse anti-GFAP, Sigma-Aldrich, #G3893, clone G-A-5: evaluated by indirect immunofluorescent staining on alcohol-fixed sections of rat brain (cerebrum or cerebellum).
3. Mouse anti-GFAP, EMD Millipore, #MAB360, clone GA5, 1:1500: routinely evaluated by Western Blot on Mouse brain lysates.

Animals and other organisms

Policy information about studies involving animals; ARRIVE guidelines recommended for reporting animal research

Laboratory animals

Adult (P56 +/- 3 days) wildtype C57Bl/6J mice, male and female

Wild animals

No wild animals were used in the study

Field-collected samples

No field-collected samples were used in the study

Human research participants

Policy information about studies involving human research participants

Population characteristics

Tissue donors used in the study:

H200.1023, 43 years old, female, Iranian descent, postmortem donor
H200.1025, 50 years old, male, Caucasian, postmortem donor
H200.1030, 54 years old, male, Caucasian, postmortem donor
H16.24.010, 66 years old, male, Caucasian, postmortem donor
H16.06.002, 35 years old, female, Caucasian, neurosurgical donor, epilepsy
H16.06.008, 24 years old, female, Hispanic, neurosurgical donor, epilepsy
H16.06.009, 48 years old, female, Caucasian, neurosurgical donor, epilepsy
H16.03.004, 25 years old, male, race unknown, neurosurgical donor, epilepsy and tumor removal

Recruitment	Postmortem specimens: Postmortem tissue specimens from males and females between 18 – 68 years of age with no known history of neuropsychiatric or neurological conditions ('control' cases) were considered for inclusion in this study of cell transcriptional profiles. Key conditions for exclusion were: • Known brain injury, cancer or disease • Known neuropsychiatric or neuropathological history • Epilepsy or other seizure history • Drug/alcohol dependency • > 1 hour on ventilator • Positive for infectious disease • Prion disease • Chronic renal failure • Death from homicide or suicide • Sleep apnea • Time since death (postmortem interval, PMI) > 25 hours Neurosurgical specimens: Tissue procurement from neurosurgical donors was performed outside of the supervision of the Allen Institute at local hospitals, and tissue was provided to the Allen Institute under the authority of the IRB of each participating hospital. A hospital-appointed case coordinator obtained informed consent from donors prior to surgery.

Flow Cytometry

Plots

Confirm that:

☒ The axis labels state the marker and fluorochrome used (e.g. CD4-FITC).

☒ The axis scales are clearly visible. Include numbers along axes only for bottom left plot of group (a 'group' is an analysis of identical markers).

☒ All plots are contour plots with outliers or pseudocolor plots.

☒ A numerical value for number of cells or percentage (with statistics) is provided.

Methodology

Sample preparation	Microdissected tissue pieces were placed in into nuclei isolation medium containing 10mM Tris pH 8.0 (Ambion) , 250mM sucrose, 25mM KCl (Ambion), 5mM MgCl2 (Ambion) 0.1% Triton-X 100 (Sigma Aldrich), 1% RNasin Plus, 1X protease inhibitor (Promega), and 0.1mM DTT in 1ml dounce homogenizer (Wheaton). Tissue was homogenized using 10 strokes of the loose dounce pestle followed by 10 strokes of the tight pestle and the resulting homogenate was passed through 30µm cell strainer (Miltenyi Biotech) and centrifuged at 900xg for 10 min to pellet nuclei. Nuclei were resuspended in buffer containing 1X PBS (Ambion), 0.8% nuclease-free BSA (Omni-Pur, EMD Millipore), and 0.5% RNasin Plus. Mouse anti-NeuN conjugated to PE (EMD Millipore) was added to preparations at a dilution of 1:500 and samples were incubated for 30 min at 4°C. Control samples were incubated with mouse IgG1,k-PE Isotype control (BD Pharmingen). Samples were then centrifuged for 5 min at 400xg to pellet nuclei and pellets were resuspended in 1X PBS, 0.8% BSA, and 0.5% RNasin Plus. DAPI (4', 6-diamidino-2-phenylindole, ThermoFisher Scientific) was applied to nuclei samples at a concentration of 0.1µg/ml.
Instrument	Single nucleus sorting was carried out on either a BD FACSAria II SORP or BD FACSAria Fusion instrument (BD Biosciences)
Software	BD Diva Software V8.0
Cell population abundance	We intentionally sorted ~10% NeuN-negative (non-neuronal) and ~90% NeuN-positive (neuronal) nuclei to enrich for neurons.
Gating strategy	Nuclei were first gated based on size (forward scatter area, FSC-A) and granularity (side scatter area, SSC-A). B, Nuclei were then gated on DAPI fluorescence, followed by gates to exclude doublets and aggregates (FSC-single cells, SSC-single cells). E, Lastly, nuclei were gated based on NeuN PE ignal (NeuN-PE-A) to differentiate neuronal (NeuN+) and non-neuronal (NeuN-) nuclei.

☒ Tick this box to confirm that a figure exemplifying the gating strategy is provided in the Supplementary Information.